

Structure-Function Relations Underlying Charge Transfer In Organic Photovoltaic Systems

by
Jacob Ryan Tinnin

A dissertation submitted to the Department of Physics,
College of Natural Sciences and Mathematics
in partial fulfillment of the requirements for the degree of

Doctor of Philosophy

in Physics

Chair of Committee: Margaret S. Cheung

Committee Member: Eric R. Bittner

Committee Member: Shuo Chen

Committee Member: Pavan Hosur

Committee Member: Oomman K. Varghese

University of Houston
December 2021

Copyright 2021, Jacob Ryan Tinnin

DEDICATION

This dissertation is dedicated to my parents, all four of them. They have always instilled a love of learning in me and made me feel I could do anything.

This dissertation is dedicated to my three brothers, whose examples I am still trying to live up to. Each of them has individually inspired me in unique ways.

This dissertation is dedicated to my wife, without whom I would never last a week. Her input is present in nearly every page of this dissertation.

ACKNOWLEDGEMENTS

This dissertation would not be possible without the contributions of many individuals. I will highlight those of just a few here. First, I would like to thank my advisor: Dr. Margaret Cheung. When I arrived at the University of Houston, I had a vague sense of what I wanted to accomplish during my time in graduate school. I was so lucky to receive an offer to join her group before my first day of class. I cannot imagine going through graduate school with a different advisor. Thanks to her guidance, I have not only grown immensely as a scientist but also as a person.

Second, I would like to thank the other members of my committee: Drs. Eric Bittner, Shuo Chen, Pavan Hosur, and Oomman Varghese. Each of them has put in time to help shape the research comprising this dissertation and deserve their place on the title page. Thank you to each of you for all of your comments and suggestions.

Third, I would like to thank Dr. Pengzhi Zhang. Thanks to him I came into a project with great groundwork already done. From day one he was a mentor to me and was always took time to give a thought-out answer to any scientific or technical question.

Fourth, I would like to thank the other co-authors on my papers: Drs. Barry Dunietz, Eitan Geva, Xiang Sun, Srijana Bhandari, Huseyin Aksu, Buddadev Maiti, and Zhengqing Tong. We have spent many hours together in meetings and editing papers. I hope you all have enjoyed working together as much as I have.

Fifth, I would like to thank the members of the Cheung group with whom I have overlapped: Drs. Jaebeom Han, Fabio Zegarra, Millad Ghane, Jacob Ezerski, Yossi Eliaz, and Andrei Gasic as well as future Drs. James Liman, Chengxuan Li, and Jules Nde. We've made it

through a hurricane, floods, a pandemic, and all the rigors of graduate school together. I look forward to all you accomplish in the future.

Last, I would like to acknowledge the funding for these projects from the U.S. Department of Energy, Basic Energy Sciences through the Chemical Sciences, Geosciences and Biosciences Division (No. DE-SC0016501). All the work here made heavy use of the computational resources are provided by the National Energy Research Scientific Computing Center, a U.S. Department of Energy Office of Science User Facility operated under Contract No. DE-AC02-05CH11231, as well as the uHPC (NSF Award Number OAC 1531814) and Sabine clusters managed by the Research Computing Data Core at the University of Houston. I am grateful for the funding and resources that made this all possible.

ABSTRACT

Organic photovoltaics (OPV) is an emerging solar cell technology with great potential advantages such as low-cost manufacturing, transparency, and solution processability. However, the performance of OPV devices is still prohibitively low, requiring a better understanding of the impact of molecular-level morphology on OPV function. This is challenging as OPV systems can have complex electronic structures and molecular morphologies. Here I show how a combination of scientific methods, for which I led the development, accurately measured CT at these different levels.

In Chapter 1, I provide background information on organic solar cells as well as on some of the methods used to study them. Next, in Chapter 2, I detail the results of applying these methods to the SubPC/C₆₀ system. The explicit treatment of solvent molecules identified a new type of molecular geometry and improves on the rate estimates given in past literature. Chapter 3 features the new open-source software CTRAMER which is a modular combination of state-of-the-art computational methods from molecular dynamics, electronic structure, and transition-rate theory. Chapter 4 covers how applying CTRAMER and physics-guided machine learning to the DBP/C₇₀ system showed that the condensed phase stabilizes a wide variety of geometries, each with unique charge transfer characteristics.

Finally, Chapter 5 outlines how these results show the importance of accounting for explicit environmental effects when studying charge transfer in organic solar cells. Furthermore, in both systems studied, simulations showed that the interface is dominated by sub-optimal geometries as well as the clear link between molecular morphology and charge transfer performance. These findings should guide the future design and manufacture of organic solar cells.

TABLE OF CONTENTS

DEDICATION.....	iii
ACKNOWLEDGEMENTS	iv
ABSTRACT.....	vi
TABLE OF CONTENTS	vii
LIST OF TABLES	ix
LIST OF FIGURES	x
CHAPTER 1. INTRODUCTION.....	1
A. Importance of charge transfer in organic photovoltaic cells.....	1
B. Molecular dynamics	3
i. Energy minimization and equilibration	4
ii. Molecular dynamics simulations for population analysis	6
iii. Population analysis using energy landscape theory and physics-guided machine learning	6
iv. Molecular dynamics simulations for rate calculations	8
C. Electronic structure	8
D. Transition rate theory	12
CHAPTER 2. MOLECULAR ANALYSIS OF SUBPC/C₆₀ CHARGE TRANSFER.....	17
A. Introduction.....	17
B. Methods.....	20
i. Molecular dynamics simulations	20
ii. Electronic structure calculations.....	25
iii. Rate constants	25
C. Results	28
i. Interfacial pair geometries	28
ii. Electronic structure of SubPC/C ₆₀ pairs	32
iii. Interfacial charge-transfer rates	39
iv. Effect of deposition protocols.....	44
D. Discussion	50
E. Conclusions	52
CHAPTER 3. CTRAMER: AUTOMATING THE ANALYSIS OF CHARGE TRANSFER.....	53
A. Introduction.....	53

B. CTRAMER methodology.....	54
i. Softwarization flow.....	56
ii. Computational Approach.....	58
iii. Electronic structure calculations (Modules 1 and 3).....	60
iv. Molecular dynamics simulations (Modules 2 and 4).....	61
v. Rate evaluations (Module 5).....	63
C. Results.....	65
i. Sample preparation (Module 1).....	66
ii. Condensed-phase structures (Module 2).....	66
iii. Electronic structure results (Module 3).....	69
iv. Charge-transfer rate constants (Modules 4 and 5).....	71
D. Conclusions.....	75
CHAPTER 4. MOLECULAR ANALYSIS OF DBP/C₇₀ CHARGE TRANSFER.....	76
A. Introduction.....	76
B. Methods.....	80
i. Electronic structure calculations.....	80
ii. System preparation and molecular dynamics simulations for population analysis.....	81
iii. Population analysis using energy landscape theory and physics-guided machine learning.....	81
iv. Molecular dynamics simulations for rate calculations.....	82
v. Rate calculations using the linearized semi-classical approximation.....	82
C. Results.....	83
i. Impact of molecular symmetry on DBP/C ₇₀ energy landscape.....	83
ii. Complex electronic structure of DBP/C ₇₀	85
iii. The $[I, I]$ geometry possesses the fastest rate but lowest population.....	87
D. Discussion.....	90
E. Conclusions.....	91
CHAPTER 5. CONCLUSIONS AND FUTURE WORK.....	92
BIBLIOGRAPHY.....	95

LIST OF TABLES

Table 2.1.	Parameters for SubPC boron atom that were not included in GAFF.....	22
Table 2.2.	Energy correction term, W_a , for each excited state.....	27
Table 2.3.	Orbital energies (eV) of <i>on-top</i> , <i>hollow</i> and <i>edge</i> geometries.....	33
Table 2.4.	Excited states properties from key donor and acceptor states of each SubPC/C ₆₀ pair geometry	37
Table 2.5.	Charge-transfer rate constants and relevant parameters for each representative geometry	41
Table 2.6.	Marcus theory parameters for all three geometries.....	42
Table 2.7.	LSC-level parameters for each transition's Gaussian distribution(s).....	43
Table 2.8.	Charge transfer rate densities (ω^C in nA/nm ²) for the five deposition models	49
Table 3.1.	Interfacial charge-transfer rates for the three SubPC/C ₆₀ representative pair geometries.....	74
Table 4.1.	Charge-transfer rate densities for the four DBP/C ₇₀ representative pair geometries	89

LIST OF FIGURES

Figure 1.1.	Excited state diagram of charge transfer dynamics in an OPV system.	2
Figure 1.2.	Example OPV system before and after equilibration.	5
Figure 1.3.	Example diagram of crowded molecular environment surrounding a DBP molecule (blue).	7
Figure 1.4.	Adapted “Jacob’s Ladder” DFT functional classification scheme.	11
Figure 1.5.	Example non-Gaussian probability density function for $U(R)$	15
Figure 2.1.	Representative geometries and order parameters of SubPC/C ₆₀ dimers.	18
Figure 2.2.	Kullback-Leibler divergence for each of the five models.	24
Figure 2.3.	The potential of mean force (a) and population of pair geometries (b) for the SubPC/C ₆₀ pair in model V.	29
Figure 2.4.	The potential of mean force for the SubPC/C ₆₀ pair in all five models.	31
Figure 2.5.	The orbital energy diagram for the three representative SubPC/C ₆₀ geometries.	34
Figure 2.6.	Excited state properties of the three representative SubPC/C ₆₀ pair geometries.	36
Figure 2.7.	The detachment and attachment electron densities of the <i>on-top</i> EX1 and bCT1 states.	38
Figure 2.8.	The five initial conditions for the deposition models used in the MD simulations.	45
Figure 2.9.	Interfacial SubPC/C ₆₀ pairs for the five deposition models.	47
Figure 3.1.	The overall workflow for CTRAMER (illustrated on the SubPC/C ₆₀ system).	55
Figure 3.2.	Flowchart representing information flow during each section of the software.	57
Figure 3.3.	Execution of the CTRAMER scripts in order.	59
Figure 3.4.	The potential of mean force (a) for the SubPC/C ₆₀ pair on a R - θ coordinate system.	68
Figure 3.5.	Excited state properties for the three SubPC/C ₆₀ representative pair geometries.	70
Figure 3.6.	A ridgeline plot of the probability density functions of $U(R)$	72
Figure 4.1.	DBP/C ₇₀ pairs are selected from an explicit condensed-phase environment to account for the effect of molecular morphology on charge transfer.	77
Figure 4.2.	DBP (a) and C ₇₀ (b) molecules with the cylindrical coordinate system (c) used to define order parameters.	79
Figure 4.3.	The potential of mean force for the DBP/C ₇₀ pair on a Z - Φ cylindrical coordinate system.	84
Figure 4.4.	Excited state properties of DBP/C ₇₀ representative pair geometries.	86
Figure 4.5.	Charge transfer rate constants (k^M) for the donor-to-acceptor transitions in each representative DBP/C ₇₀ geometry.	88

CHAPTER 1. INTRODUCTION

A. Importance of charge transfer in organic photovoltaic cells

With the rise of environmental problems from energy production, the need for sustainable energy continues to grow. Photovoltaic (PV) devices turn light into electricity via the photovoltaic effect. PV devices are made up of semiconducting cells, which are known as solar cells when using light from the Sun. PVs now count for over 2% of the world's energy supply and that figure is expected to grow rapidly.¹ The majority of PV devices consist of crystalline silicon and other inorganic materials. However, a rising area of research focuses on solar cells based on organic material.^{1,2}

Research on organic photovoltaic (OPV) devices is motivated by their low production and environment costs, improved plasticity, and synthetic tunability in comparison to inorganic PVs.³⁻¹⁶ However, the current efficiency of leading OPV cells is much lower than that of leading inorganic PV cells.^{1,2,17} Additionally, many OPV devices suffer from photodegradation.

Within OPV devices, photoexcitation of the donor material leads to the formation of excitons. The excitons then diffuse to the donor/acceptor (D/A) interface, where charge transfer (CT) from donor to acceptor occurs.^{3-5,18} This is followed by charge separation, where the electron and hole diffuse away from the interface within the donor and acceptor layers, respectively. Thus, a better understanding of the correlation between the effect of varying interfacial D/A pair geometries on CT rate constants is required to improve OPV performance.^{3,8,19-22}

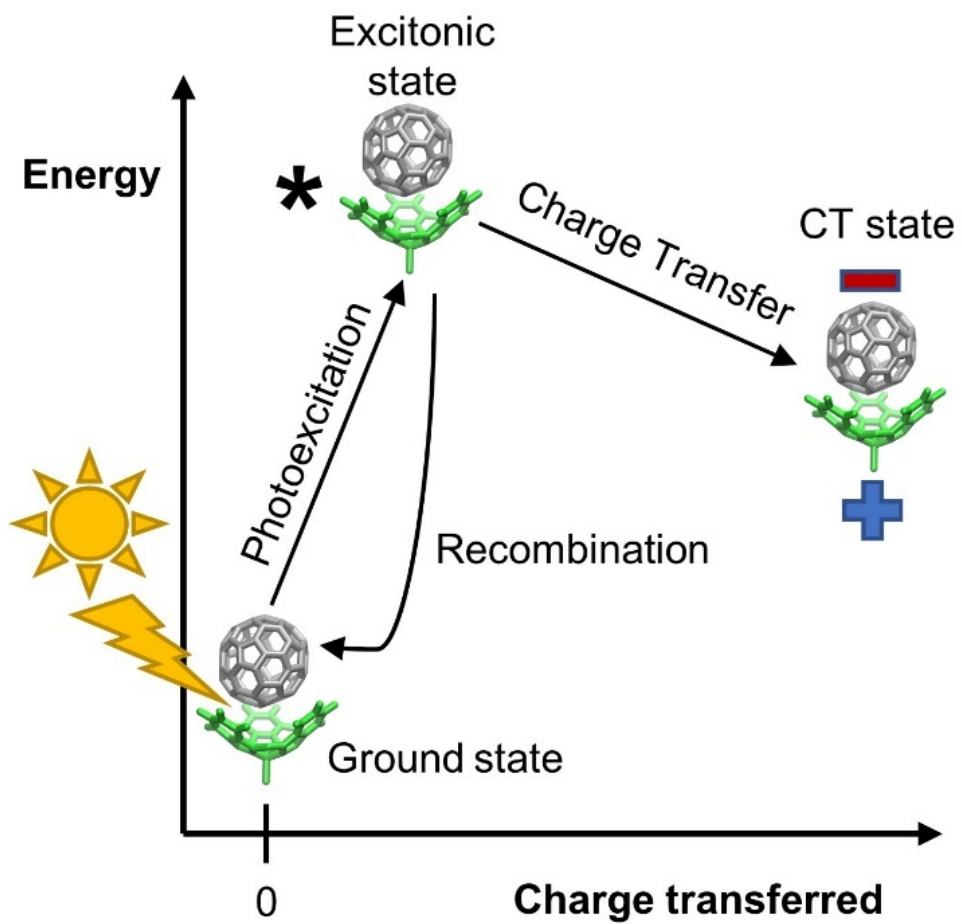


Figure 1.1. Excited state diagram of charge transfer dynamics in an OPV system.

In this dissertation, I investigated two example OPV systems. First, an OPV cell consisting of boron subphthalocyanine (SubPC) as the electron D and a fullerene (C_{60}) as the electron A^{4,6,8,23-26} that continues to draw a wide research effort as a model of OPV systems.^{14,25-28} This research interest motivates its use by me as well as the fact that SubPC/ C_{60} cell parameters have been shown to depend on the fabrication scheme and surface morphology.^{6,8,29,30} Second, an OPV cell consisting of Tetraphenyldibenzoperiflanthen (DBP) as the electron D and a fullerene (C_{70}) as the electron A. The DBP/ C_{70} cell is well-studied system with unique geometries and a complex electronic structure.^{31,32} Previous studies of the correlation between interfacial structure and CT rates in these systems, as well as other similar systems, have been based on the optimal geometries of D-A pairs embedded in a polarized continuum model (PCM),^{4,23,28,31,33} which can only account for the effect of the solid-state host in a mean-field manner which can't account for these changes in surface morphology.

B. Molecular dynamics

Molecular dynamics (MD) is a computational method that solves Newton's classical equations of motion for a system of particles, which can each represent one or more atoms, using numerical integration. The system is allowed to evolve over time forming what is known as a trajectory. Time averages over the course of a trajectory are used to estimate physical parameters. The numerical methods allow for MD to handle a large number of atoms. However, the classical nature of MD means that chemical reactions can't be accurately studied. Additionally, MD requires the definition of a potential function.

Empirical-based potential functions are known as force fields, which consists of parameters such as atomic charges and bond angles. For non-polarizable force fields, these parameters are set

for the length of the simulation while for polarizable force fields they are allowed to change over time. Recent work has showed that the choice of electronic structure method (covered in Chapter 1.C) is more important than using a polarizable force field.³⁴ The MD simulations in this dissertation utilized the AMBER software and its generalized AMBER force field (GAFF).³⁵⁻³⁸

i. Energy minimization and equilibration

A hybrid algorithm was used to perform energy minimization. The conjugated-gradient method was used for 500 timesteps, followed by 4500 timesteps of the steepest-descent method. The minimized system was then heated to 298.15K using the canonical ensemble (NVT) gradually over a period of 10 ps, then the system was fixed at this temperature for 1.0 ns and equilibrated at a constant pressure of 1.0 bar using an NPT ensemble with 1.0 ps as the pressure relaxation time. The simulation box was then refit to the equilibrated system (an example is shown in Figure 1.2) with periodic boundary conditions kept.

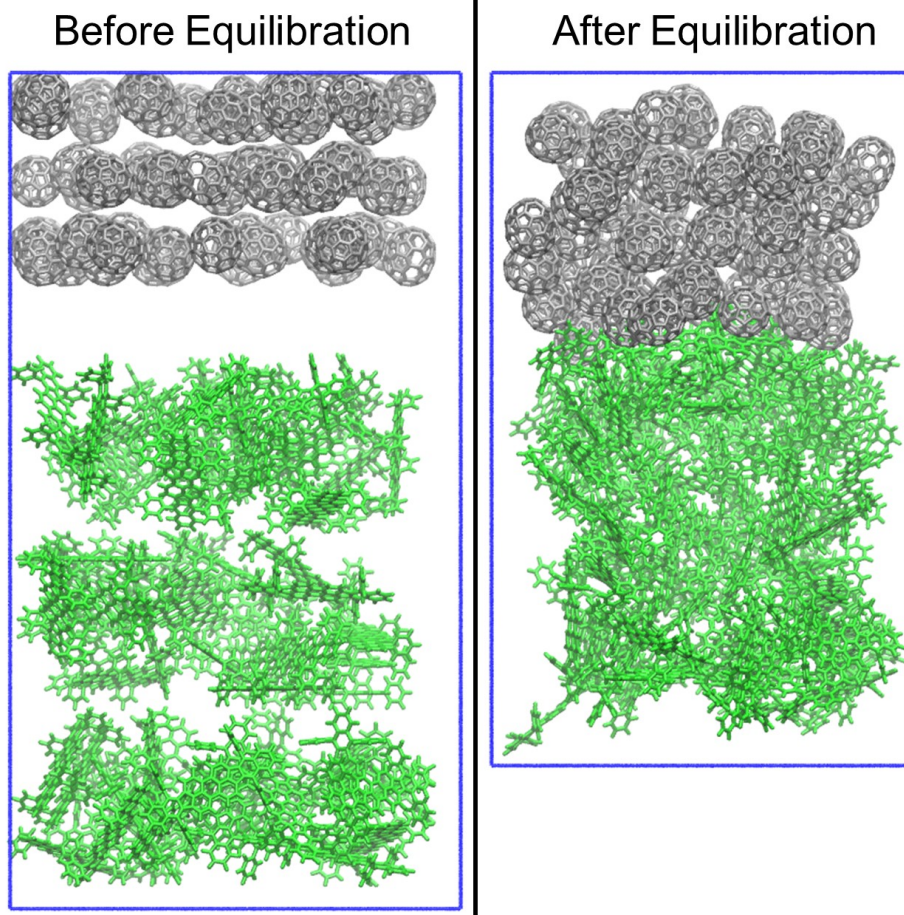


Figure 1.2. Example OPV system before and after equilibration. The blue rectangle represents the periodic boundary. The system shown is DBP/ C_{70} with DBP in green and C_{70} in gray.

ii. Molecular dynamics simulations for population analysis

The MD simulations were performed by the AMBER program SANDER,³⁷ fitting the simulation box to the constructed system and then applying periodic boundary conditions. Both equilibration and production MD simulations had a time step of 2.0 fs. The SHAKE algorithm³⁹ was used to constrain bonds involving hydrogen. Neighbor list updates, real-space Coulomb interactions, and van der Waals interactions utilized a 10.0 Å threshold. Electrostatic interactions were modeled with the particle-mesh Ewald method.^{40,41} Production runs for population analysis were run on the equilibrated system (shown in Figure 1.2) with the adjusted box size in a NVT ensemble.

iii. Population analysis using energy landscape theory and physics-guided machine learning

Interfacial D/A pairs were sampled from the MD production runs with an interfacial D/A pair defined as 1 donor molecule and 1 acceptor molecule where the minimum distance between any atom from separate molecules was less than 5 Å. The pairs were then characterized using order parameters based on the symmetry of each molecule. For the SubPC/C₆₀ system, spherical coordinates R and θ were used while cylindrical coordinates Z and Φ were used for the DBP/C₇₀ system. For both coordinate systems, location refers to the location of the center of mass of the acceptor molecule while the origin is set at the SubPC's boron atom and the center of mass of the DBP molecule. As shown in Figure 1.3, in the condensed phase molecules tend to neighbor several molecules and, therefore, each molecule can be involved in multiple D/A pairs. For the methodology detailed in this dissertation I treated each pair separately.

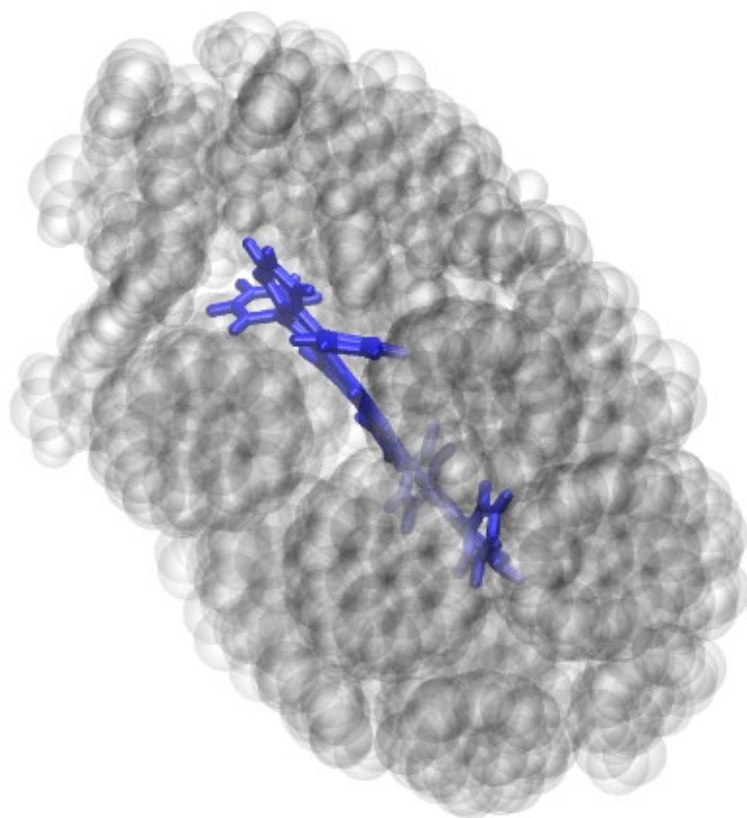


Figure 1.3. Example diagram of crowded molecular environment surrounding a DBP molecule (blue).

The probability density was then estimated using 2D kernel density estimation.^{42,43} The bandwidth was optimized⁴⁴ individually for each variable to minimize L2 loss, or mean integrated squared error. The density at the boundaries of support was corrected using the reflection method.⁴⁵ From this density estimate, the free energy was calculated using the Boltzmann approximation.

iv. Molecular dynamics simulations for rate calculations

Production runs for rate calculations used the entire system in the timestep from which a representative geometry was chosen. The atoms of the representative pair were fixed in place using a harmonic potential with a force constant of 50 kcal/mol-Å². As the energies calculated by AMBER do not include the restraint potential, changing the size of this force constant would not affect the results.^{34,37} The goal of fixing the atoms is to keep the molecules in the representative geometry. These fixed atoms were assigned with Mulliken partial charges of a donor state for that representative pair geometry. The rest of the molecules in the system had ground state charges and were unrestrained. All other parameters were the same as for MD simulations for population analysis.

C. Electronic structure

Electronic structure refers to the motion of electrons relative to stationary nuclei. The separation of electron motion and nucleus motion is known as the Born-Oppenheimer approximation. The electronic structure problem is finding the stationary state solutions to the time-independent Schrödinger equation. Solving this problem is crucial as Dirac showed that all properties of a ground state can be expressed as a function of the electron density.⁴⁶ Hohenberg, Kohn, and Sham further reduced the intractable many-body problem of interacting electrons to

noninteracting electrons in an effective potential.⁴⁷⁻⁴⁹ This is exact, in principle, but the exact kinetic energy functional from the electron density is not known. These principles are the basis for density functional theory (DFT).^{48,50-52} Runge and Gross showed that the same applies for low-lying excited states,⁵³ allowing for an extension to DFT known as time-dependent density functional theory (TD-DFT) to model excited states.^{52,54} The following paragraphs thus use DFT to refer equally to both DFT and TD-DFT.

Research on DFT focuses on finding improvements to kinetic energy functionals, particularly in modelling exchange and correlation interactions. In outlining the types of functionals I here use a “Jacob’s Ladder” shown in Figure 1.4 as proposed by Perdew,^{55,56} with adaptations to focus on recent advances that aid in accurately modelling CT states. Many other types of functionals exist beyond what are mentioned here. The first two rungs utilize just the electron density (local spin density approximation, LSDA) and its gradient (generalized gradient approximation, GGA) to model the kinetic energy but are not accurate enough to have widespread use in chemistry. The third rung introduces hybrid functionals, which add a constant amount of exchange energy from Hartree-Fock (HF) theory. While both “hybrid LSDA” and “hybrid GGA” functionals exist, hybrid GGAs are used much more. B3LYP, a hybrid GGA, is the most commonly used DFT functional.^{57,58}

A specific area where DFT struggles is with CT excitations, particularly over different molecules.^{34,59-61} These excitations require full HF exchange in the large D/A distance limit but hybrid functionals use only a fraction (typically around 25%). This is solved using “range-separated” hybrid functionals, RSHs, that utilize a fraction of HF exchange in the “short range” and full HF exchange in the “long range.”⁶²⁻⁶⁴ Unfortunately, results have been shown to be extremely sensitive to the choice of range-separation parameter, ω , where the shift from short

range to long range is done.^{60,62,65,66} To combat this, Baer et al. introduced a “tuning” algorithm for the BNL functional that optimizes ω based on the system.⁶⁷⁻⁷¹ This allows RSHs to be accurate and system-specific but still non-empirical. The BNL functional was used for the results in Chapters 2 and 3. Chapter 4 utilizes a “screened range-separated hybrid” (SRSH) which utilizes the relative permeability of the system to obtain the correct asymptotic potential.⁷²⁻⁷⁴

Adapted Jacob's Ladder of DFT Functionals

1. LSDA (Local Spin-Density Approximation)
 - ρ_σ , electron (spin-) density
2. GGA (Generalized Gradient Approximation)
 - $\nabla\rho_\sigma$
3. Global hybrid
 - Adds a constant fraction of "exact" Hartree-Fock exchange
4. RSH (Range-Separated Hybrid)
 - Splits exchange into short-range and long-range components
5. Tunable RSH
 - Tunes the range-separation parameter in a system-specific way
6. SRSH (Screened Range-Separated Hybrid)
 - "Screens" the long-range exchange according to dielectric response

Figure 1.4. Adapted "Jacob's Ladder" DFT functional classification scheme. The class of functionals at each "rung" incorporates all the elements from the previous rung plus the additional element listed below its name. This scheme was taken from ^{55,56} and adapted to focus on recent advances (rungs 4-6) that aid in modelling charge-transfer states.

All electronic structure calculations in this dissertation were performed using Q-Chem.⁵² TD-DFT was used on interfacial D/A molecule pairs selected from MD to obtain excited states and their partial charges, oscillator strength (OS), and relative energy.⁵³ The electronic structure protocols used in this dissertation have been benchmarked against experimentally measured excitation energies⁷⁵⁻⁷⁷ (including those of charge-transfer states) as well as measured rates.^{4,78}

Important excited states were selected and then classified as donor and/or acceptor states as follows. First, the charge of the donor molecule, Q_D , was used to classify states either as non-CT or CT (the threshold Q_D value used for each system is given in the methods of that chapter). Second, states with a significant OS were classified as light-absorbing states, or *bright*.⁷⁹ CT states with negligible OS were classified as *dark* (dCT) and those with a significant OS as bright CT (bCT). Non-CT states with significant OS were referred to as excitonic (EX). As this dissertation focuses on direct CT from photoexcited (bright) states to CT states, states that are both dark and non-CT were not addressed. The states were then named as EX n , bCT n , or dCT n . The index n refers to the rank of a state's energy, from smallest to largest, within EX, bCT, and dCT states with the same geometry.

Last, using these classified states, transitions from a bright state to a CT state were selected. As part of these electronic structure calculations, electronic coupling coefficients were computed for each transition using the fragment-charge-differences (FCD) method.⁸⁰

D. Transition rate theory

CT rates are often calculated by and rationalized within the framework of Marcus theory.⁸¹⁻
⁸⁵ Marcus theory's appeal lies in the fact that the Marcus CT rate constant can be expressed in terms of only three parameters—the electronic coupling coefficient (Γ_{DA}), the reorganization

energy (E_r), and the reaction free energy (ΔE). This makes fitting and understanding experimentally measured CT rate constants simple. However, the restrictive nature of the assumptions underlying Marcus theory also makes it highly desirable to develop more comprehensive methods for calculating CT rates,⁸⁶ in particular for systems whose Hamiltonian are given in terms of anharmonic force fields. This would allow for computing CT rate constants directly without mapping it onto an effective harmonic model Hamiltonian.⁸⁷⁻⁸⁹

My collaborators and I have recently developed and tested such a general and direct strategy for calculating CT rate constants in complex molecular systems described by general anharmonic force fields.^{3,16,85,86,90} Our approach starts out by applying the linearized semiclassical (LSC) approximation to the equilibrium Fermi’s golden rule (FGR) expression for the CT rate constant.^{3,86,91-93} The classical-like nature of the LSC-based FGR expression implies that it can be applied to complex molecular systems governed by anharmonic force fields of one’s choice. At the same time, the LSC-based FGR expression has been shown to reproduce the quantum-mechanically exact rate constant when the donor and acceptor potential energy surfaces are parabolic and identical except for shifts in equilibrium geometry and equilibrium energy.

Transition rate constants in this dissertation were calculated following a Marcus-level LSC approximation, where the donor-to-acceptor transition rate constant (k^M) is given by:

$$k^M = \frac{|\Gamma_{DA}|^2}{\hbar} \sqrt{\frac{2\pi}{\sigma_U^2}} \exp\left[-\frac{\langle U \rangle^2}{2\sigma_U^2}\right]. \quad (1.1)$$

Here, $U(\mathbf{R}) = V_D(\mathbf{R}) - V_A(\mathbf{R})$ is the D/A energy gap as a function of the nuclear coordinates, \mathbf{R} , where V_D and V_A are the potential-energy surfaces of the donor and acceptor states, respectively. $\langle U \rangle$ and σ_U are the first and second moments, respectively, of $U(\mathbf{R})$. This rate constant was derived from FGR by the LSC approximation, as detailed in refs.^{86,92,94,95}, but is here referred to as “Marcus-level” as the reorganization energy, E_r , the reaction free energy, ΔE , and

the activation energy, E_a , can be calculated from $\langle U \rangle$ and σ_U : $E_r = \sigma_U^2 / (2k_B T)$, $\Delta E = -E_r - \langle U \rangle$, and $E_a = k_B T \langle U \rangle^2 / (2\sigma_U^2)$. These parameters allow for the analysis of rates calculated using Marcus Theory.⁸¹⁻⁸⁴

$U(\mathbf{R})$ was determined for each transition using classically sampled trajectories of a D/A pair fixed in place with donor state charges. Then, the potential energy surface at a given timestep in a trajectory, V_α^M , was calculated for each state, with α denoting the donor or the acceptor, by recalculating the energy of the entire system in AMBER12.³⁷ To avoid double counting of potential energy by the electronic structure and MD methods, V_α^M was corrected to $V_\alpha = V_\alpha^M + W_\alpha$, where W_α is the difference in single-point energy of each state between calculations by the electronic structure and MD methods. U was then determined using the difference of V_D and V_A . Finally, $\langle U \rangle$ and σ_U were obtained using the moments of N_R MD trajectories of length L_R .

As shown in Figure 1.5, the distribution of $U(\mathbf{R})$ can be significantly non-Gaussian for many transitions.^{3,16} I attribute this to the CTRAMER process accounting for how the condensed phase's heterogeneity can lead to multiple local energy minima. As the LSC approximation uses a Gaussian distribution to model the probability density at $U(\mathbf{R}) = 0$, these energy minima were resolved by best fitting the probability density function of $U(\mathbf{R})$ to a sum of Gaussian distributions chosen by least-squares regression. The number of distributions was then increased, beginning at one, until the 95% confidence interval for σ_U includes non-positive numbers or a maximum of three is reached.

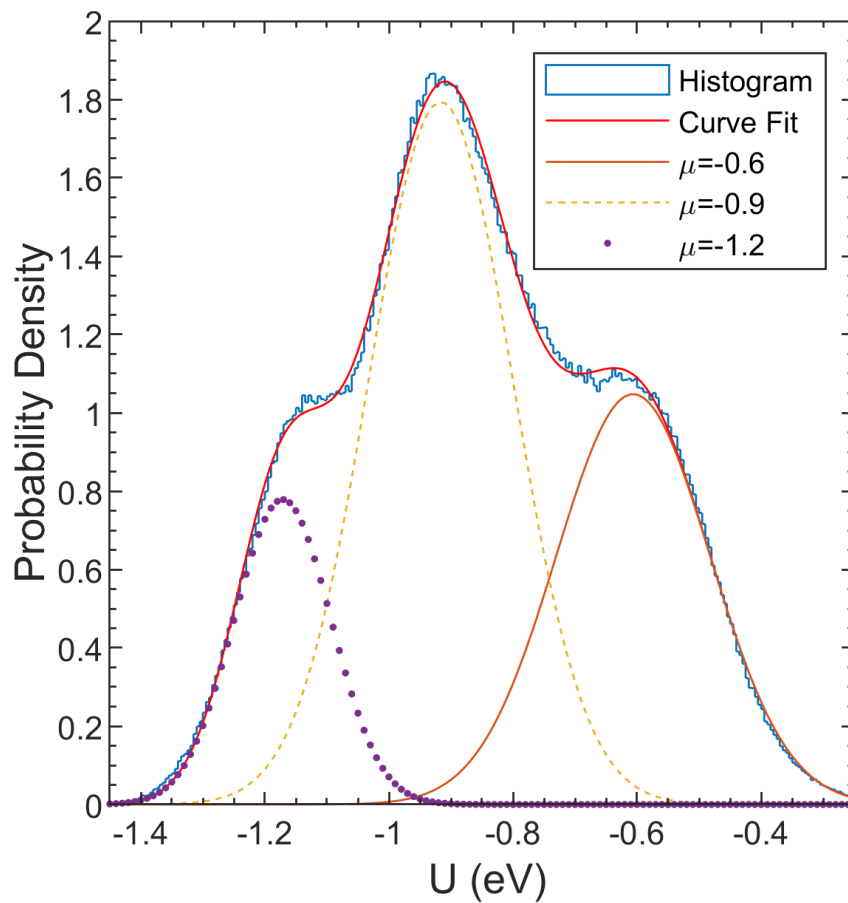


Figure 1.5. Example non-Gaussian probability density function for $U(\mathbf{R})$. The three Gaussian functions used to fit the distribution of $U(\mathbf{R})$ are shown. The distribution shown here is taken from the EX1 \rightarrow dCT1 transition for the *hollow* SubPC/ C_{60} geometry.

While k^M measures the transition rate between states, I multiplied it by the amount of the corresponding charge transferred, (ΔQ_D), to measure the rate of CT (k^C) for a transition:

$$k^C = \Delta Q_D k^M. \quad (1.2)$$

Both k^C and k^M were obtained in the context of a single transition for one structure. For aid in comparison between structures, these CT rates were summed over all the identified transitions, t , for a given representative structure i , to give a structure-level CT rate constant (K_i^C or K_i^M):

$$K_i^C = \sum_t k_t^C. \quad (1.3)$$

A system-level CT density (ω^C) was then established with a weighted average of K_i^C over the area of the D/A interface in the simulation:

$$\omega^C = \sum_i (K_i^C n_i) \times \frac{1}{A}, \quad (1.4)$$

where n_i is the number of pairs per timestep represented by the structure i from Equation 1.3 and A is the approximate area of the interface.

CHAPTER 2. MOLECULAR ANALYSIS OF SUBPC/C₆₀

CHARGE TRANSFER

Adapted from: Tinnin J, *et al.* Molecular-Level Exploration of the Structure-Function Relations Underlying Interfacial Charge Transfer in the Subphthalocyanine/C₆₀ Organic Photovoltaic System. *Phys Rev Appl* **13**, 11 (2020).

A. Introduction

In this chapter, I investigate the relationship between interfacial structure and CT rates in an OPV cell consisting of boron subphthalocyanine (SubPC) as the electron D and fullerene (C₆₀) as the electron A.^{4,6,8,23-26} The SubPC/C₆₀ cell continues to draw a wide research effort as a model of OPV systems.^{14,25-28} For example, the SubPC/C₆₀ cell parameters have been shown to depend on the fabrication scheme and surface morphology.^{6,8,29,30} The goal of this chapter is twofold. First, I aim to provide insights on the relationships between interfacial structure and CT kinetics and to develop a comprehensive computational framework that will be implemented to design OPV cells of enhanced efficiencies. I hope that the lessons learned from the study of the model system will inspire new design strategies of OPV cells. Second, the computational framework as reported here is expected to play a role in the search for such enhanced OPV applications.

While, previous studies of the correlation between interfacial structure and CT rates in the SubPC/C₆₀ system and similar phthalocyanine-fullerene systems have been based on the optimal geometries of D-A pairs embedded in a polarized continuum model (PCM),^{4,23,28,31,33} which can only account for the effect of the solid-state host in a mean-field manner. These earlier studies identified two key interfacial donor-acceptor pair geometries, referred to as *on-top* and *hollow* (see Figures 2.1(a), 2.1(b), respectively) which correspond to the cases in which the concave and convex sides of SubPC (bowl-shaped) face C₆₀ (spherical), respectively.

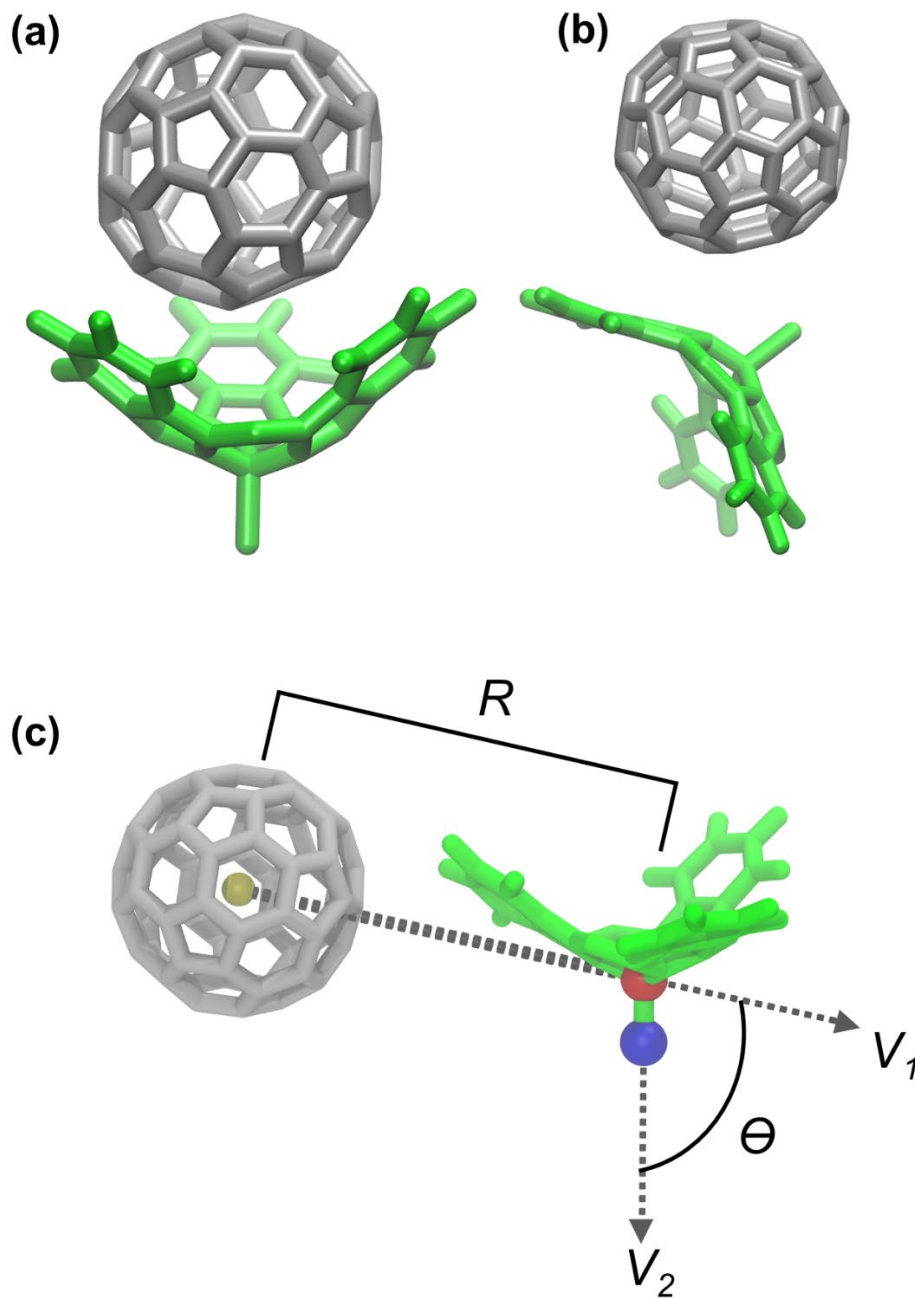


Figure 2.1. Representative geometries and order parameters of SubPC/ C_{60} dimers. There are three representative donor-acceptor pair geometries: (a) on-top, (b) hollow, and (c) edge. Order parameters are defined in (C), where the yellow bead corresponds to the center of mass of the C_{60} , and the red and blue beads correspond to the boron and chlorine atoms of SubPC, respectively. Order parameter, R , is the distance between the center of mass of C_{60} and the boron atom. Order parameter, θ , is the angle between the two vectors, V_1 and V_2 , shown in the diagram.

Importantly, a mean-field modeling at the PCM level cannot account for the many-body effects brought about by the nonuniform molecular nature of the solid-state environment.^{19,85,96} More specifically, the optimal D-A pair geometries may not be representative of the actual geometries found in a solid-state system. Furthermore, treating the environment as a dielectric continuum cannot account for the fact that there is likely a distribution of geometries, rather than a few well-defined ones.

I used classical all-atom molecular-dynamics (MD) simulations to obtain an ensemble of interfacial D-A pair geometries. In doing so, I found that the ensemble of geometries is dominated by a third type of pair geometry, which I refer to as “*edge*” (see Figure 2.1(c)), in addition to the *on-top* and *hollow* geometries.

I also investigated how type of geometry, overlooked by earlier gas-phase or PCM calculations, impacts CT rates. To this end, my collaborators performed electronic structure calculations on three representative D-A pair geometries and I used those results to calculate the distribution of rate constants at the Marcus-theory level (k^M).⁸⁶ The resulting rates were comparable to previously reported experimental and calculated rates.^{4,28,33} I also defined the corresponding CT rate constant (k^C) as the product of k^M and the charge (ΔQ_D) associated with the CT transition. I found that the amount of charge transferred depends significantly both on the D-A pair geometry and the particular transition involved. While the CT rates were key in determining the cell performance, the rates for other processes involved in the charge separation and collection had to be also determined.^{14,15}

The fabrication protocol, where the order of the layer deposition is varied, has been shown to impact the device performance and therefore presumably the underlying ensemble of interfacial geometries.^{8,97} I addressed such variant distributions of the interfacial pairs by using extreme cases

in setting up the MD simulations to elaborate on the potential impact of the fabrication protocol to enhance the device parameter. For the different cases, MD simulations were analyzed to obtain the statistical weight (p) of each geometry for each model. This allowed for measuring the CT rate density (ω^C) for a given model, by summing pk^C for each geometry. Therefore, ω^C allowed for quantifying the correlation between interfacial morphology and CT rates. As presented below, I found that maximizing the *on-top* population enhances the performance.

B. Methods

i. Molecular dynamics simulations

In order to examine the effect of fabrication procedures on the interfacial structure, I considered five different sets of initial conditions (see Figure 2.8) constructed by my collaborator Dr. Pengzhi Zhang using a combination of AMBER³⁸ and PACKMOL:⁹⁸

- **Model I Stacked layers(*on-top*):** Three layers of C₆₀ molecules were stacked on three layers of SubPc molecules in the same orientation, where the inside of SubPC molecules faced C₆₀ molecules, similar to the “*on-top*” configuration in Figure 2.1(a). All molecules are aligned on a $5 \times 5 \times 6$ grid.
- **Model II Stacked layers (*hollow*):** Same as Model (I), but the SubPC molecules were aligned that the outside of SubPC molecules faced C₆₀ molecules, similar to the “*hollow*” configuration in Figure 2.1(b).
- **Model III Alternating layers (on grid):** Three layers of C₆₀ molecules were mixed with three layers of SubPC molecules alternatively on a $5 \times 5 \times 6$ grid. The SubPC molecules were aligned in the same orientation in every layer.

- **Model IV Stacked layers (disordered):** Three layers of C₆₀ molecules were stacked on three layers of SubPC molecules. Each layer consisted of 25 C₆₀ or SubPC molecules, whose positions and orientations were optimized by Packmol.⁹⁸
- **Model V Alternating layers (disordered):** Three layers of C₆₀ molecules were mixed with three layers of SubPC molecules alternatively. Each layer consisted of 25 C₆₀ or SubPC molecules, whose positions and orientations were optimized by Packmol.⁹⁸

MD simulations were performed on each model following the guidelines in Chapter 1.B. with the initial size of the simulation box for each model varying depending on the initial configurations (with the box size after equilibration approximately 60 Å × 60 Å × 80 Å for all five models). Interactions involving the boron atom for SubPC were not provided in GAFF and were therefore adopted from Refs ^{99,100} and AMBER Antechamber^{35,36} (see Table 2.1). “Na” in the table uses the notation of GAFF, which refers to an sp² Nitrogen atom with three bonds. The partial charge of boron atom was assigned by neutralizing the net charge of a SubPC molecule.

Table 2.1. Parameters for SubPC boron atom that were not included in GAFF

	Cl-B (Å)	B-Na (Å)	N-B-N (°)	Cl-B-N (°)	B-N-C (°)	σ_B (Å)	ϵ_B (kcal/mol)	Charge (<i>e</i>)
Parameters	1.863	1.467	105.2	113.8	122.5	2.010	0.095	1.3465
Source	99	99	99			100	100	

A 20 ns constant volume and temperature production run was performed for each model. Convergence of the production runs was achieved as the Kullback-Leibler (K-L) divergence,¹⁰¹ also known as surprisal,¹⁰² between distributions of the total potential energy of the system over accumulative simulation time approaches zero at 20 ns (see Figure 2.2). K-L divergence between the probability distribution P (reference) and Q as a function of the order parameter x is defined as follows:

$$\Gamma(P, Q) = - \sum_x P(x) \ln \frac{Q(x)}{P(x)}. \quad (2.1)$$

The K-L-divergence analysis indicates a well-sampled trajectory if the changes between distributions at different times are small. A value of zero indicates that the two distributions are identical. I systematically calculated the K-L divergence between the distributions of accumulated trajectories at a simulation time interval of 1 ns. The results of my analysis indicated that simulations for all deposition models reached convergence since the K-L divergence between potential energy distributions approached zero by the end of my simulation runs.

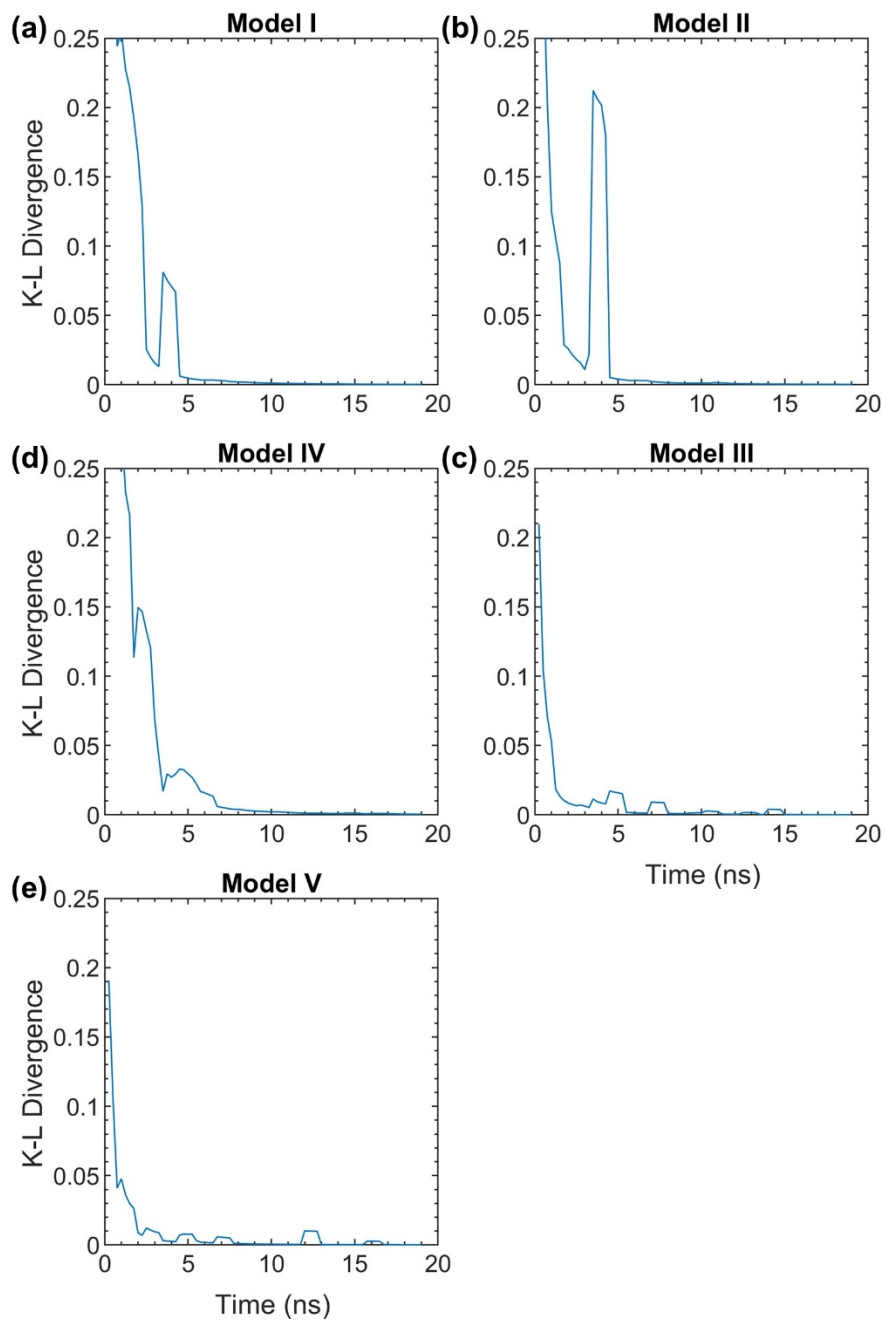


Figure 2.2. Kullback-Leibler divergence for each of the five models. A lower divergence indicates a lesser difference in the potential energy distribution when additional simulation time is added.

ii. Electronic structure calculations

All electronic structure calculations were performed within Q-Chem 4⁵² by my collaborators Drs. Srijana Bhandari, Huseyin Aksu, and Buddahev Maiti following the guidelines in Chapter 1.C. Excited state electronic structure calculations were performed via time-dependent density functional theory (TD-DFT) on selected donor-acceptor pairs.⁵³ The Baer–Neuhauser–Livshits (BNL) range-separated hybrid functional^{67,68} and the 6-31G* basis set¹⁰³ were used. An optimally tuned γ of 0.167 bohr⁻¹, obtained based on the J2(γ) scheme⁶⁹ for the *on-top* geometry, was used in all calculations.

Electronic excited states were classified based on the charge of the donor molecule, Q_D , either as non-CT states ($Q_D < 0.10 e$) or CT states ($Q_D > 0.10 e$). The non-CT states and CT states were denoted as EX n and CT n , respectively. The index n is used to order the states within a class by their energy, from lowest to highest. CT states with a significant oscillator strength (OS),⁷⁹ were referred to as light-absorbing or *bright* (bCT) whereas CT states with negligible OS were referred to as *dark* (dCT).

iii. Rate constants

CT rate constants and densities were calculated using an adapted LSC method as detailed in Chapter 1.D. $\langle U \rangle$ and σ_U for a given transition were calculated from NVT MD simulations. Using the coordinates and velocities of a completed trajectory, V_D^M and V_A^M were found by recalculating the energy of the entire system using MD, as denoted by M. To address double counting between the electronic structure and MD calculations, I defined $V_\alpha = V_D^M + V_A^M$, where W_α is the energy correction and α denotes a donor or aceptor state. W_α was computed as the difference of the single-point energy for each state of the SubPC/C₆₀ pair between quantum

chemistry calculations and MD simulations in Table 2.2. For each D-to-A transition, U was calculated by finding the difference of V_D and V_A at each time step of 1 ps. Then, $\langle U \rangle$ was obtained by averaging over 40 MD trajectories (40 ns each).

The reorganization energy, E_r , reaction free energy, ΔE , and activation energy, E_a , can be expressed in terms of $\langle U \rangle$ and σ_U : $E_r = \frac{\sigma_U^2}{2k_B T}$, $\Delta E = -E_r - \langle U \rangle$, and $E_a = k_B T \frac{\langle U \rangle^2}{2\sigma_U^2}$. These are listed in Table 2.6 for each transition.

As shown in Figure 1.5, the distribution of $U(\mathbf{R})$ was not Gaussian. This was attributed to different solid-state environments that correspond to different local minima which were resolved by best fitting the distribution of $U(\mathbf{R})$ to a sum of Gaussian distributions. The distributions were chosen by least-squares fitting, with the number of Gaussian distributions chosen to be three unless the confidence intervals of the standard deviation contain negative numbers. If not, it was decreased until that criterion was satisfied. These parameters are listed in Table 2.7.

Table 2.2. Energy correction term, W_a , for each excited state

Geometry	State	$W_a(\text{eV})$
<i>On-top</i>	EX1	-36.0634
	bCT1	-36.0004
	dCT1	-36.3159
	dCT2	-36.3116
	dCT3	-36.0420
<i>Hollow</i>	EX1	-37.5764
	dCT1	-37.6803
	dCT2	-37.6421
	dCT3	-37.6776
<i>Edge</i>	EX1	-37.2171
	dCT1	-37.2666
	dCT2	-37.1928
	dCT3	-37.2104

C. Results

i. Interfacial pair geometries

Classical all-atomistic MD simulations were performed at 298.15K within a periodic cubic box containing 75 C₆₀ and 75 SubPC molecules for 20 ns. The simulation box was prepared using five different deposition models to probe the wide range of possible fabrication procedures (see the detailed discussion below in Chapter 2.B.i for the initial setup of the layer). An ensemble of interfacial D-A pairs, defined as when the closest distance between any atom in C₆₀ and any atom in SubPC is no more than 5 Å, was then obtained. The potential of mean force (PMF) was calculated by categorizing the pairs based on two order parameters [see Figure 2.1(c)]: (1) R , which is the distance between the center of mass of C₆₀ and the boron atom of SubPC; and (2) θ , which is the angle between the vector from the center of mass of C₆₀ to the boron atom of SubPC and the vector from the boron atom to the chlorine atom of SubPC.

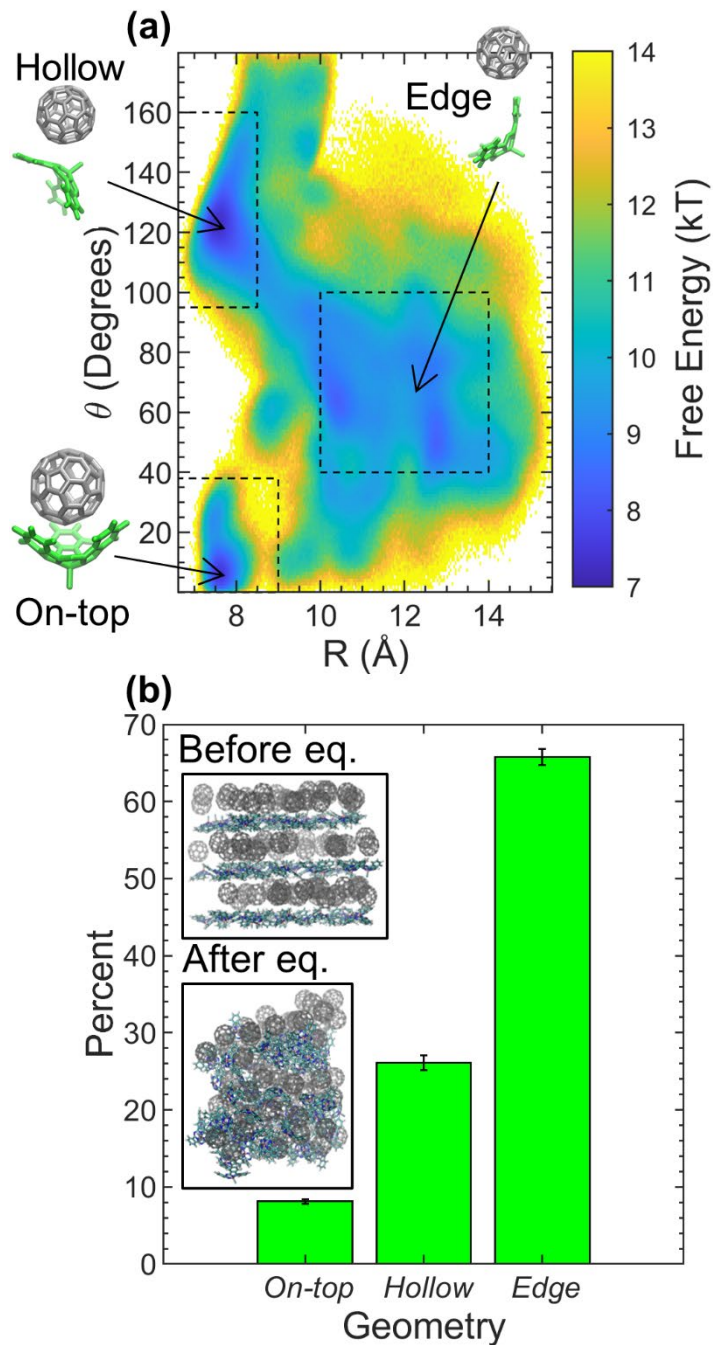


Figure 2.3. The potential of mean force (a) and population of pair geometries (b) for the SubPC/ C_{60} pair in model V. The order parameters R and θ are defined in Figure 1.1(c). The color is scaled by $k_B T$. The corresponding ranges of the order parameters for the different spatial pairs are indicated by the rectangular boxes. On top, $R < 8.5 \text{\AA}$ and $\theta < 38^\circ$; hollow, $R < 9 \text{\AA}$ and $95^\circ < \theta < 160^\circ$; edge (the majority), $10 \text{\AA} < R < 14 \text{\AA}$ and $40^\circ < \theta < 100^\circ$. Also shown are representative geometries (on top, hollow, and edge) of SubPC/ C_{60} at each of the three major basins. The setup of deposition model V is shown both before and after equilibration as insets in (b). For the other deposition models introduced below, see Figure 2.8.

Inspection of the PMF for Model V in Figure 2.3 reveals two pronounced basins centered at $(R, \theta) = (7.5 \text{ \AA}, 0^\circ)$ and $(R, \theta) = (7.5 \text{ \AA}, 120^\circ)$, which correspond to the *on-top* [Figure 2.1(a)] and *hollow* [Figure 2.1(b)] pair geometries, respectively. The corresponding basins on the PMF were defined as $R < 8.5 \text{ \AA}$ and $\theta < 38^\circ$ for *on-top* pairs and $R < 9 \text{ \AA}$ and $95^\circ < \theta < 160^\circ$ for *hollow* pairs. The PMFs for all five models are shown in Figure 2.4.

I also found a third broad basin on the PMF that does not correspond to either previously identified geometry for interfacial SubPC/C₆₀ pairs. This basin consisted of pairs where only the *edge* of SubPC is in contact with C₆₀. I here refer to this previously overlooked D-A pair geometry as *edge*. The basin for the *edge* geometry corresponded effectively to anything that is not *on top* or *hollow*. The majority of the *edge* pairs fell within the following range: $10 \text{ \AA} < R < 14 \text{ \AA}$ and $40^\circ < \theta < 100^\circ$. While *edge* geometries had a wide variance in θ , I selected one structure as an example to aid visualization, as shown in Figure 2.1(c) and Figure 2.3(a). It should be noted that although the *edge* basin was shallow compared to the *hollow* and/or *on-top* basins, it covered a significantly larger area in the R - θ plane. As a result, the *edge* population was actually larger than that of *on top* or *hollow* [see Figure 2.3(b)]. I note that an overwhelming majority of around 90% of all molecules at the interface were involved in more than a single interfacial pair. This, however, does not affect the CT kinetics on the macroscopical scale, which effectively follow the larger rate constants.

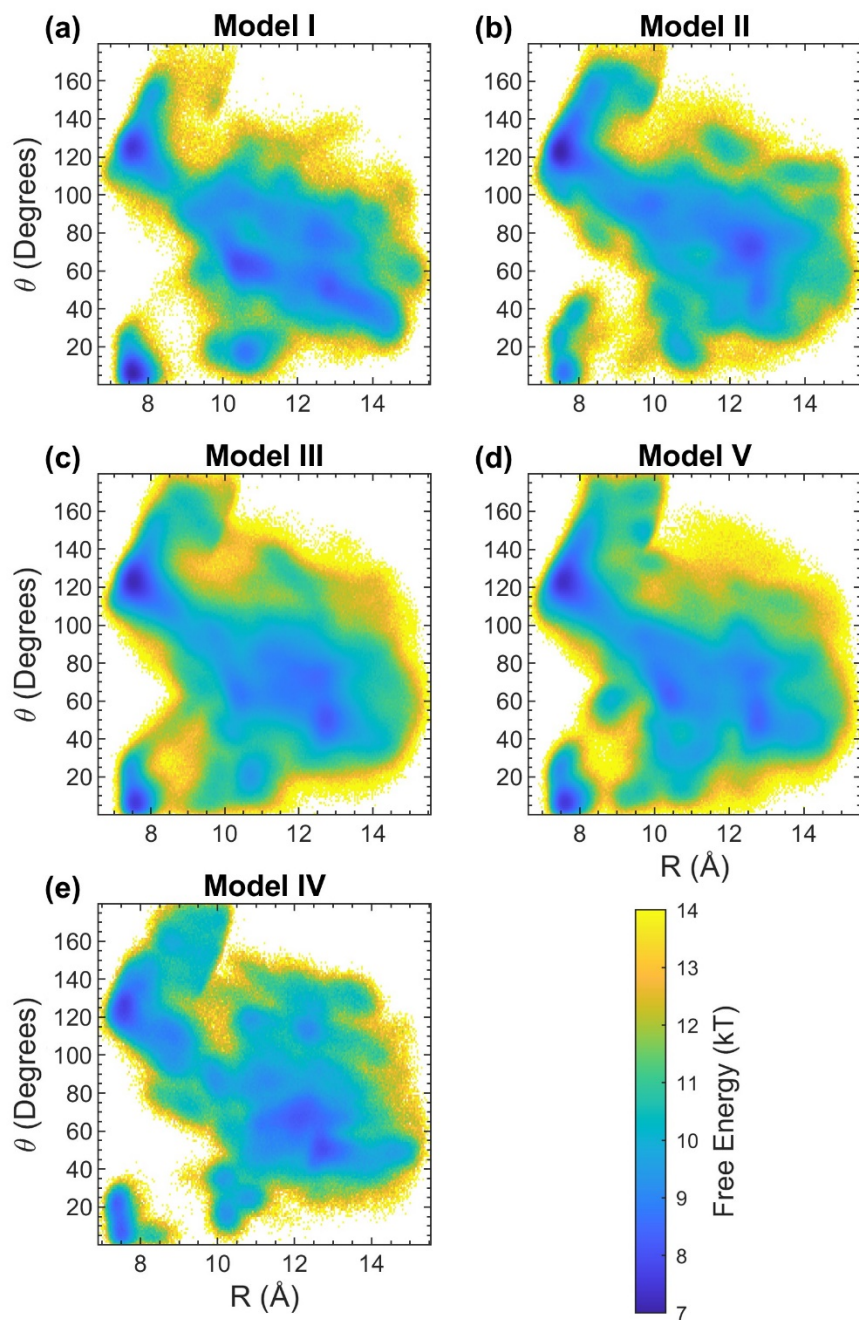


Figure 2.4. The potential of mean force for the SubPC/C₆₀ pair in all five models. The order parameters R and θ are defined in Figure 2.1(c). The color is scaled by $k_B T$. For the setup of each model, see Figure 2.8.

ii. Electronic structure of SubPC/C₆₀ pairs

Three representative D-A pair geometries that correspond to the *on-top*, *hollow*, and *edge* subensembles were selected. Electronic structure calculations were performed on them as described in Chapter 2.B.ii. Figure 2.5 shows that the low-lying excited states in SubPC/C₆₀ pairs involved the highest occupied molecular orbital (HOMO) of SubPC and the lowest unoccupied molecular orbital (LUMO) of either SubPC or C₆₀. More specifically, in all three geometries, the HOMO, HOMO-1, LUMO+3 and LUMO+4 were localized on SubPC (the donor molecule), while the LUMO, LUMO+1 and LUMO+2 were localized on C₆₀ (the acceptor molecule) (see the molecular orbital energies listed in Table 2.3). Considering the coupling of the low-lying excitation localized on the donor to a CT state, my collaborators found that the HOMO and LUMO+3 on the donor are key in the donor state and the LUMOs of all the pairs localized on the acceptor are key in the CT state (see these orbitals highlighted in Figure 2.5).

Table 2.3. Orbital energies (eV) of *on-top*, *hollow* and *edge* geometries

Orbitals	Configuration		
	On-top	Hollow	Edge
HOMO-1	-6.340	-6.177	-6.449
HOMO	-5.959	-5.987	-5.851
LUMO	-1.633	-1.415	-1.633
LUMO+1	-1.542	-1.306	-1.578
LUMO+2	-1.252	-1.252	-1.497
LUMO+3	-0.898	-1.034	-0.707
LUMO+4	-0.626	-0.762	-0.626

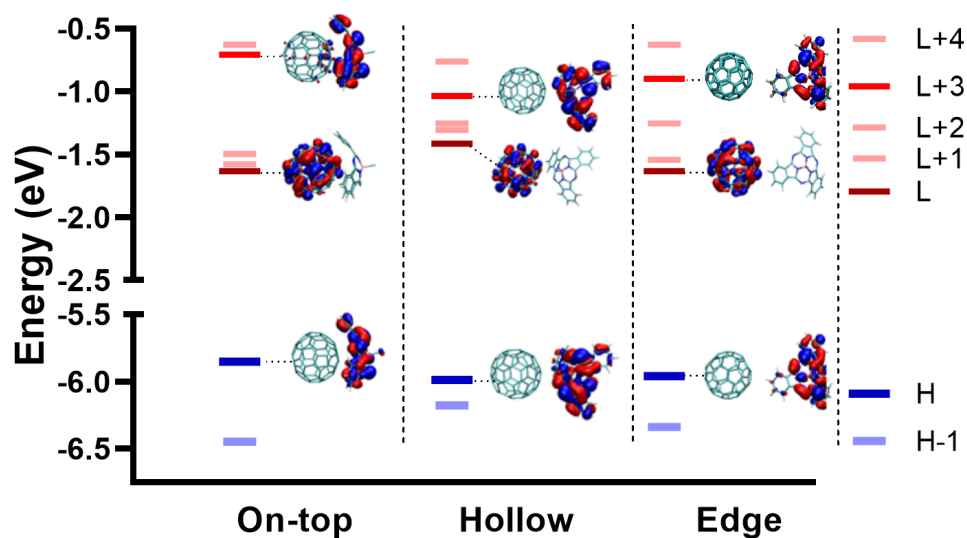


Figure 2.5. The orbital energy diagram for the three representative SubPC/C₆₀ geometries. The pair's HOMO, shown in blue and denoted as "H," is localized on SubPC. The pair's LUMO, shown in red and denoted as "L," is localized on C₆₀ and contributes to all the CT states. The absorbing excited state involves the LUMO on the donor, which is the pair's LUMO+3 shown in red. For the *on-top* geometry, we found an additional absorbing state where the LUMO+4 plays a role (the LUMO+1 on the donor). Figure by Drs. Srijana Bhandari, Huseyin Aksu, and Buddahev Maiti.

I next considered the excited state properties by following their energies within the isolated pair (E^{gas}), oscillator strength (OS), and the charge of the donor molecule (Q_{D}) (see Figure 2.6). States were designated as bright (light absorbing) if they possess significant OS⁷⁹ or dark if associated with low OS values. Bright absorbing excitonic states (EX) and CT states also were distinguished by their Q_{D} , where the CT states possess $Q_{\text{D}} > 0.10 e$. The values of OS and energies of the main orbitals involved in individual states are listed in Table 2.4. States were ordered as $n = 1, 2, 3, \dots$ according to ascending gas-phase excitation energy, E^{gas} .

I focused on transitions from the bright EX state with the highest OS to dark CT (dCT) states, with one exception: in the *on-top* geometry I considered a second bright absorbing state that is also a charge-transfer state (bCT), for which both the Q_{D} and OS are significant. While the EX1 states for the *edge* and *hollow* geometries involved the LUMO on the donor (LUMO+3 of the pair), for the *on-top* geometry this corresponded to the bCT1 state and the LUMO+4 ws involved in the EX1 state. The detachment and attachment densities of the bCT1 and EX1 states are shown in Figure 2.7. For all the geometries, I considered several dark charge transfer states, the dominant orbital transitions of which are indicated in Table 2.4.

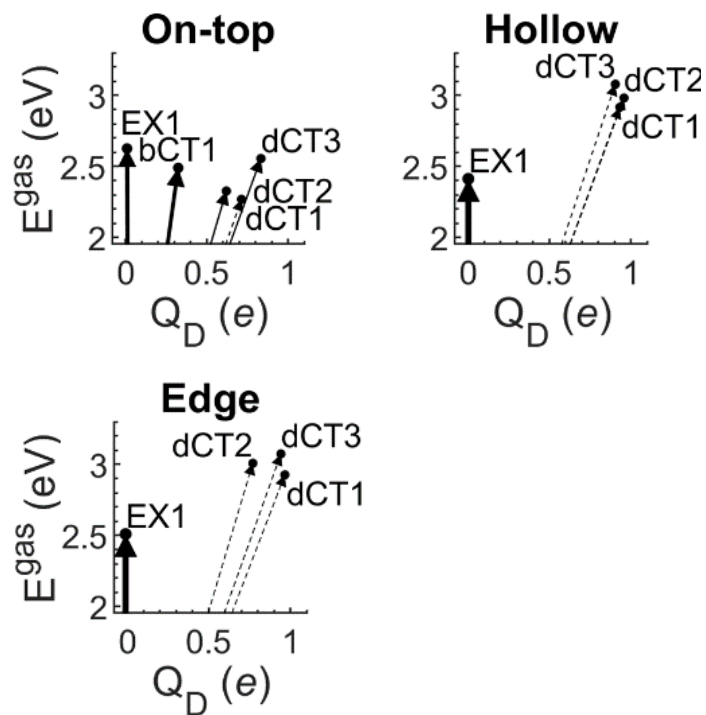


Figure 2.6. Excited state properties of the three representative SubPC/C₆₀ pair geometries. The x axis measures the charge of the donor molecule (Q_D) in units of e and the y axis measures the excitation energy (E^{gas}) in units of electronvolts. The oscillator strength (OS) is represented by the arrow width. States with a vanishing OS are represented by a thin dotted line. The numerical values are listed in Table 2.4.

Table 2.4. Excited states properties from key donor and acceptor states of each SubPC/C₆₀ pair geometry

	Donor states		Acceptor states		
On-top	bCT1	EX1	dCT1	dCT2	dCT3
OS	0.11	0.13	0.00	0.02	0.02
Q_D (e)	0.32	0.00	0.71	0.62	0.83
E^{gas} (eV)	2.495	2.626	2.269	2.327	2.557
Main orbital replacements	H→L+3(0.79)	H→L+4(0.92)	H→L(0.64)	H→L+1(0.61)	H→L+3(0.72)
Hollow	EX1	EX2	dCT1	dCT2	dCT3
OS	0.26	0.20	0.00	0.00	0.00
Q_D (e)	0.00	0.00	0.93	0.96	0.90
E^{gas} (eV)	2.411	2.538	2.917	2.982	3.079
Main orbital replacements	H→L+3(0.95)	H→L+4(0.94)	H→L(0.72), H→L+2(0.48)	H→L+1(0.86), H→L(0.33)	H→L+2(0.78), H→L(0.46)
Edge	EX1	EX2	dCT1	dCT2	dCT3
OS	0.26	0.27	0.00	0.00	0.00
Q_D (e)	0.01	0.01	0.97	0.77	0.94
E^{gas} (eV)	2.509	2.559	2.927	3.008	3.074
Main orbital replacements	H→L+4(0.85), H→L+3(0.42)	H→L+4(0.86), H→L+3(0.41)	H→L(0.96)	H→L+1(0.81), H→L+2(0.32)	H→L+2(0.88)

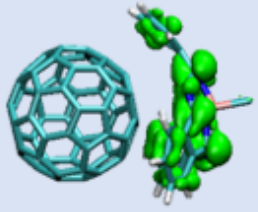
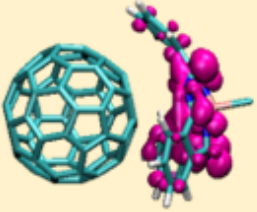
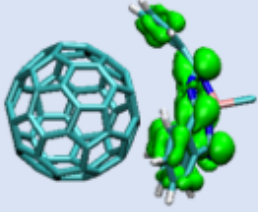
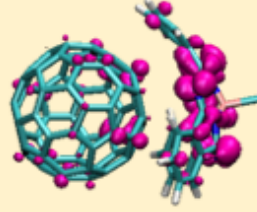
State	Detachment	Attachment
EX1		
bCT1		

Figure 2.7. The detachment and attachment electron densities of the *on-top* EX1 and bCT1 states. Here, the detachment (green) and attachment (magenta) densities demonstrate that the charge density decreased and increased relative to the corresponding electronic states, respectively. Figure by Drs. Srijana Bhandari, Huseyin Aksu, and Buddahev Maiti.

iii. Interfacial charge-transfer rates

I calculated the electronic-population-transfer rate constant, k^M , for transitions between a donor state (EX1 or bCT1) to an acceptor state (dCT1, dCT2, or dCT3) using a Marcus-like expression based on the linearized semiclassical approximation.^{85,86} The required inputs to calculate k^M , as shown in Equation 1.1 in Chapter 1.D, are a classically sampled D-A energy gap from MD as well as the coupling coefficient, Γ_{DA} , and the excitation-energy correction, W_ω , from electronic structure calculations (see Table 2.5 and Table 2.2). While most studies focus on the rate of transfer from one electronic state to another, k^M , I introduced a CT rate constant, k^C , to address transitions of varying amounts of charge transferred, ΔQ_D , particularly in transitions involving a bCT state. The rate constant, k^C , is the product of k^M and ΔQ_D (see Table 2.7). This allowed for the evaluation of a transition based on both its rate and the amount of relevant charge. The MD simulations affected the excitation energies by considering the molecular environment. Clearly, the CT states are expected to have been more stabilized than the localized excitations.⁹⁶

In the *on-top* geometry, the Γ_{DA} for the bCT1→dCT1 and bCT1→dCT2 transitions was the largest of all the coupling energies considered by a factor of two. On the other hand, ΔQ_D for transitions involving bCT1 was smaller than that of other transitions due to the higher Q_D shown in Figure 2.6. As a result, the values of k^C for transitions with EX1 and bCT1 as parent states in the *on-top* geometry were comparable (within an order of magnitude) both to each other and to previously calculated values for k^M (however, it should be noted that the states and transitions in literature do not exactly correspond to those reported here, as the geometries here were taken from MD as opposed to optimized geometries).⁴

For the *hollow* and *edge* geometries Γ_{DA} for transitions from EX1 to dCT states were smaller than any transitions for *on top* and consequently were associated with smaller rate

constants. Interestingly, the k^C values for *edge* were overall faster than those of the *hollow* geometry. This was somewhat surprising considering the relatively smaller contact between the donor and acceptor molecules in the *edge* geometry. This difference between *edge* and *hollow* can be traced back to the fact that the transitions in the *edge* geometry correspond to a much smaller $\langle U \rangle$ than those of *hollow* (see Table 2.5). The k^M for transitions in the *hollow* geometry were observed to be significantly smaller than previously reported.⁴

Table 2.5. Charge-transfer rate constants and relevant parameters for each representative geometry

Geometry	Transition	Γ_{DA} (meV)	ΔQ_D (e)	$\langle U \rangle$ (meV)	k^C (A)
<i>On-top</i>	EX1→dCT1	4.03	0.706	217±2	1.8(±0.1)x10 ⁻⁷
	EX1→dCT2	24.46	0.616	148±11	5.2(±0.7)x10 ⁻⁷
	EX1→dCT3	5.47	0.825	-168±1	2.2(±0.1)x10 ⁻⁷
	EX1→bCT1	25.82	0.314	114±5	5.1(±0.4)x10 ⁻⁷
	bCT1→dCT1	74.16	0.391	123±2	2.4(±0.2)x10 ⁻⁸
	bCT1→dCT2	72.27	0.302	61.6±0.1	1.01(±0.02)x10 ⁻⁶
bCT1→dCT3	21.13	0.511	-240± 12	1.4(±0.8)x10 ⁻¹¹	
<i>Hollow</i>	EX1→dCT1	1.85	0.943	-743±14	6(±2)x10 ⁻¹²
	EX1→dCT2	20.21	0.959	-837±14	4(±2)x10 ⁻¹¹
	EX1→dCT3	15.53	0.905	-936±30	6(±4)x10 ⁻¹²
<i>Edge</i>	EX1→dCT1	10.30	0.977	-354±23	6.5(±0.5)x10 ⁻⁸
	EX1→dCT2	14.02	0.781	-432±15	3.2(±0.7)x10 ⁻¹⁰
	EX1→dCT3	17.22	0.953	-481±20	3.1(±0.6)x10 ⁻⁹

Table 2.6. Marcus theory parameters for all three geometries

Geometry	Transition	E_r (meV)	ΔE (meV)	E_a (meV)
<i>On-top</i>	EX1→dCT1	67 ± 8	-441 ± 10	521± 67
		94.6± 0.8	-306.9± 0.9	119± 1
		20 ± 3	1 ± 4	5± 2
	EX1→dCT2	153 ± 10	-333 ± 13	52± 6
		59 ± 2	-196 ± 2	79± 3
	EX1→dCT3	98 ± 13	-126 ± 14	2± 1
		141 ± 1	33 ± 1	54± 1
		30 ± 56	439 ± 7	1832±351
	EX1→bCT1	73 ± 4	-176 ± 5	36± 3
		9.6± 0.5	-95.3± 0.8	190± 9
	bCT1→dCT1	22 ± 1	-153 ± 2	199± 12
		13.6± 0.2	-116.9± 0.3	197± 2
bCT1→dCT2	15.7± 0.4	-177.2± 0.4	415± 11	
	9.9± 0.1	-71.5± 0.1	96± 1	
bCT1→dCT3	28.4± 0.8	238 ± 2	623± 19	
	32 ± 1	324 ± 3	324± 18	
<i>Hollow</i>	EX1→dCT1	299 ± 12	197 ± 13	206± 9
		261 ± 12	545 ± 13	622± 30
		119 ± 6	942 ± 6	2366±116
	EX1→dCT2	320 ± 10	273 ± 11	275± 9
		269 ± 11	635 ± 11	761± 30
	EX1→dCT3	126 ± 5	1025 ± 6	2632±111
371 ± 25		312 ± 26	314± 22	
<i>Edge</i>	EX1→dCT1	328 ± 26	696 ± 26	799± 63
		108 ± 10	1185 ± 11	3878± 36
		191 ± 4	24 ± 5	60± 2
	EX1→dCT2	176 ± 8	264 ± 8	275± 12
		704 ± 263	-67 ± 272	145± 67
	EX1→dCT3	114 ± 3	199 ± 3	215± 5
125 ± 5		370 ± 5	490± 19	
EX1→dCT3	352 ± 103	347 ± 109	347±113	
	165 ± 4	170 ± 4	170± 4	
	188 ± 7	369 ± 7	413± 16	
		617 ± 204	177 ± 211	255± 97

Table 2.7. LSC-level parameters for each transition's Gaussian distribution(s)

Geometry	Transition	Γ_{DA} (meV)	Weight	$\langle U \rangle$ (meV)	σ_U (meV)	k^M (Hz)
<i>On-top</i>	EX1→dCT1	4.03	0.048±0.004	374 ± 5	59 ± 4	$2_{-2}^{+15} \times 10^3$
			0.938±0.005	212.3±0.4	69.7±0.2	8.6(±0.3) $\times 10^9$
			0.015±0.001	-21 ± 2	32 ± 3	1.5(±0.1) $\times 10^{12}$
	EX1→dCT2	24.46	0.29 ± 0.05	179 ± 7	89 ± 3	3.3(±0.7) $\times 10^{12}$
			0.70 ± 0.05	136.7±0.8	55 ± 1	1.9(±0.2) $\times 10^{12}$
	EX1→dCT3	5.47	0.054±0.005	28 ± 6	71 ± 5	1.5(±0.1) $\times 10^{12}$
			0.932±0.005	-174.3±0.5	85.2±0.4	1.60(±0.03) $\times 10^{11}$
			0.015±0.001	-469 ± 4	39 ± 4	0
	EX1→bCT1	25.82	0.23 ± 0.02	103 ± 2	61 ± 2	1.0(±0.1) $\times 10^{13}$
			0.25 ± 0.02	85.7±0.6	22.3±0.5	6.9(±2.3) $\times 10^{10}$
bCT1→dCT1	74.16	0.52 ± 0.03	131 ± 1	33.3±0.9	3(±1) $\times 10^{10}$	
		0.669±0.008	103.3±0.3	26.4±0.2	3.7(±0.3) $\times 10^{11}$	
bCT1→dCT2	72.27	0.332±0.008	161.5±0.7	28.4±0.4	7(±3) $\times 10^{11}$	
		1.002±0.003	61.6±0.1	22.5±0.1	2.10(±0.04) $\times 10^{13}$	
bCT1→dCT3	21.13	0.58 ± 0.04	-267 ± 2	38.3±0.5	1(±1) $\times 10^3$	
		0.42 ± 0.04	-205 ± 3	41 ± 1	1(±1) $\times 10^8$	
<i>Hollow</i>	EX1→dCT1	1.85	0.325±0.009	-496 ± 4	124 ± 3	4(±1) $\times 10^7$
			0.52 ± 0.01	-806 ± 2	116 ± 3	$4_{-3}^{+7} \times 10^0$
			0.153±0.007	-1,061 ± 3	78.2±0.2	0
	EX1→dCT2	20.21	0.327±0.008	-593 ± 3	128 ± 2	3(±1) $\times 10^8$
			0.53 ± 0.01	-904 ± 1	118 ± 2	$2_{-1}^{+4} \times 10^0$
	EX1→dCT3	15.53	0.142±0.006	-1,151 ± 3	80 ± 2	0
0.35 ± 0.02			-683 ± 7	138 ± 5	3(±3) $\times 10^7$	
<i>Edge</i>	EX1→dCT1	10.30	0.54 ± 0.02	-1,024 ± 3	130 ± 5	$2_{-2}^{+20} \times 10^{-1}$
			0.12 ± 0.01	-1,293.1±0.4	74.4±0.3	0
			0.460±0.008	-215 ± 2	99 ± 1	3.9(±0.2) $\times 10^{11}$
	EX1→dCT2	14.02	0.46 ± 0.03	-441 ± 1	95 ± 2	9(±4) $\times 10^7$
			0.08 ± 0.03	-639 ± 72	190 ± 46	$7_{-7}^{+37} \times 10^9$
EX1→dCT3	17.22	0.427±0.009	-313 ± 2	76.5±0.9	2.3(±0.5) $\times 10^9$	
		0.51 ± 0.02	-496 ± 1	80 ± 2	$5_{-3}^{+5} \times 10^4$	
		0.07 ± 0.02	-699 ± 35	135 ± 20	$8_{-1}^{+200} \times 10^6$	
		0.420±0.008	-334 ± 2	92 ± 1	1.7(±0.3) $\times 10^{10}$	
		0.51 ± 0.02	-558 ± 1	98 ± 2	1.2(±0.8) $\times 10^6$	
		0.07 ± 0.02	-794 ± 55	178 ± 29	$3_{-3}^{+43} \times 10^8$	

iv. Effect of deposition protocols

I considered five deposition models that mimic extreme scenarios of fabrication that were associated with different geometries (see Figure 2.8). Models I-III were characterized by an ordered SubPC layer upon which the C_{60} layer is deposited. The ordered SubPC layers in models I and II were arranged such that they are biased toward the *on-top* and *hollow* geometries, respectively. Model III, on the other hand, was unbiased by having alternating layers. Models IV and V were characterized by a disordered SubPC layer deposited on top of an ordered C_{60} layer. The difference between models IV and V was that model V had alternating layers.

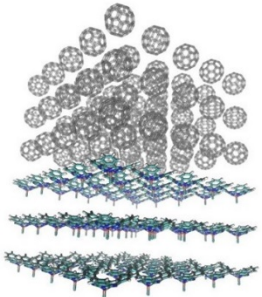
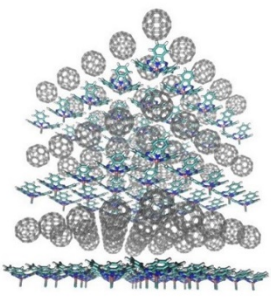
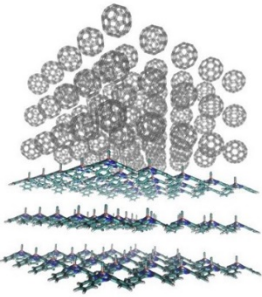
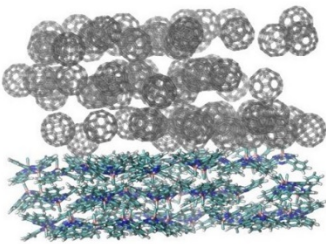
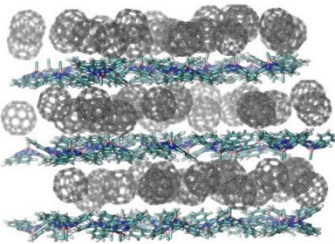
	Stacked Layers	Alternating Layers
On-top	<p>Model I</p> 	<p>Model III</p> 
Hollow	<p>Model II</p> 	
Disordered	<p>Model IV</p> 	<p>Model V</p> 

Figure 2.8. The five initial conditions for the deposition models used in the MD simulations. Each consisted of six layers of 25 SubPC or C₆₀ molecules (three SubPC layers + three C₆₀ layers). The models differed with respect to the order of layers and the orientation of the molecules in the SubPC layer. Detailed descriptions can be found in Chapter 2.B.i.

I performed MD simulations for these five models and created free-energy surfaces as shown in Figure 2.4. I then calculated the populations of the three geometries for the five models (see Figure 2.9(a)). I found that for all deposition models considered, the *edge* geometry was the dominant one. I also found that the relative population of the *on-top* versus the *hollow* geometries depended quite strongly on the deposition model. More specifically, model I (stacked layers—*on-top*) led to the highest *on-top* population while model II (stacked layers—*hollow*) had the lowest *on-top* population (see Figure 2.9(b)). Additionally, the three other models, involving alternating layers and/or random orientations in the SubPC layer, showed intermediate relative populations between models I and II.

In addition to different relative populations, each deposition model possessed a different packing density that may impact device performance. Figure 2.9(c) shows that model II, the interface of which was dominated by pairs in the *hollow* geometry, had the largest number of interfacial pairs per unit area. Model I had an interfacial pair density that, while lower than that of model II, was higher than those of models III-V. Thus, the deposition procedures that were biased towards only one geometry had higher packing density.

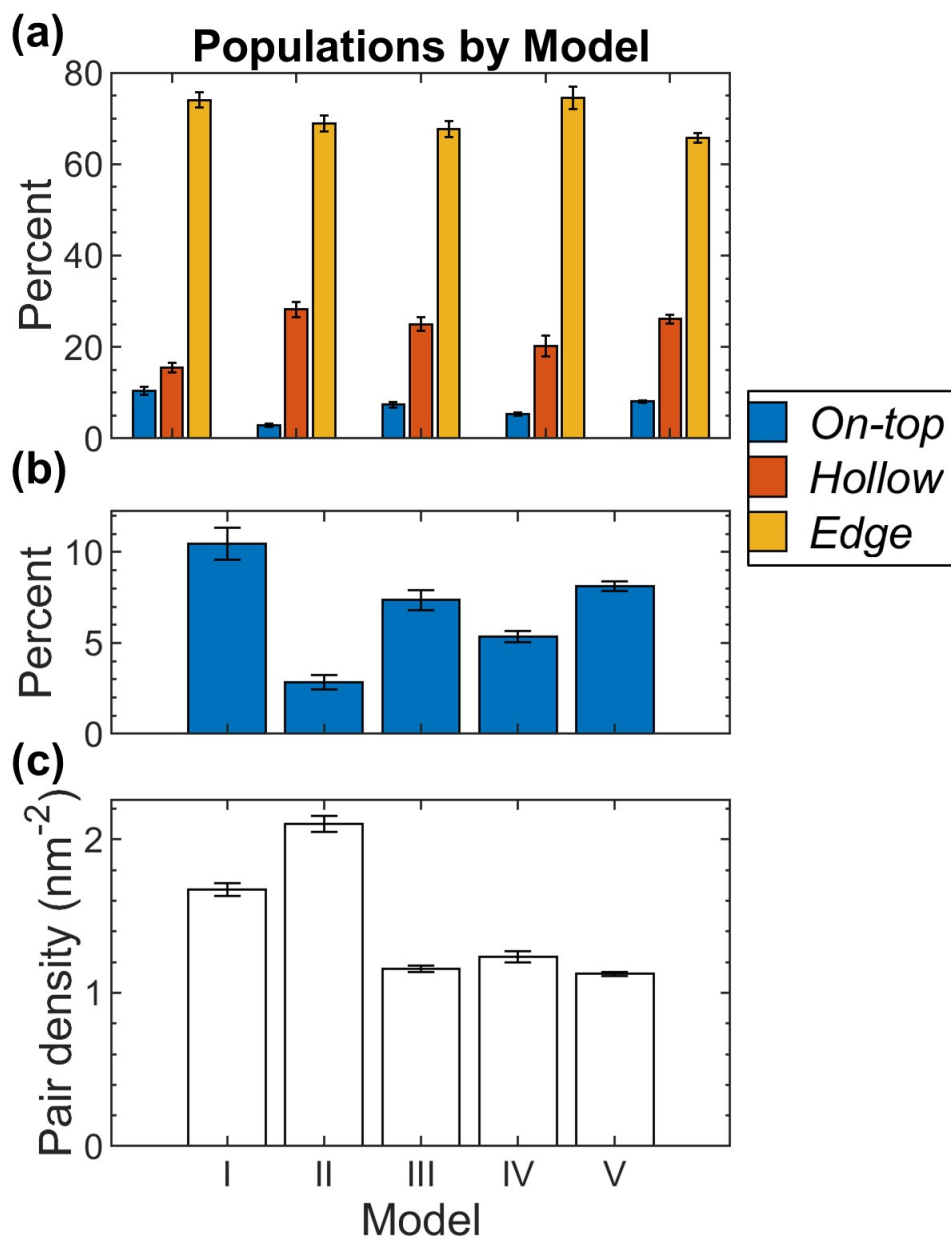


Figure 2.9. Interfacial SubPC/C₆₀ pairs for the five deposition models. (a) The percentage of interfacial pairs in the on-top (blue), hollow (red), and edge (yellow) geometries. (b) Only the percentage of interfacial pairs in the on-top geometry in each model. (c) The pair density at the interface of each model. For a diagram of the five models, see Figure 2.8.

In Table 2.8, I evaluated the expected device performance based on the deposition model in terms of CT rate density (ω^C) by considering the populations of each geometry (Figure 2.9(a)), their corresponding k^C (Table 2.5), and the pair density (Figure 2.9(c)). It should be noted that models I, II, and IV had an interfacial area five times smaller than that of Models III and V due to their alternating layers. Model I had the largest ω^C among the five deposition models because it had the largest population of pairs in the *on-top* geometry. The *on-top* geometry dominated ω^C for all deposition models due to its large k^C value, while the *hollow* geometry was nearly insignificant due to its low k^C . Interestingly, the *edge* geometry played a significant role because of its large population. As a consequence, all other deposition models gave rise to similar performance despite a lower *on-top* population.

Table 2.8. Charge transfer rate densities (ω^C in nA/nm²) for the five deposition models

ω^C (nA/nm ²)	Model I	Model II	Model III	Model IV	Model V
<i>On-top</i>	113±10	39±6	55±4	43±3	59±3
<i>Hollow</i>	0	0	0	0	0
<i>Edge</i>	37±2	43±3	23±2	27±2	22±1
Total	149±11	82±6	78±5	70±4	81±3

D. Discussion

MD simulations were used to obtain an ensemble of interfacial donor-acceptor geometries in the SubPC/C₆₀ OPV system. This molecular-level analysis should be contrasted with previous studies that were based on a dielectric continuum mean-field level of modeling and have yielded only two interfacial geometries (on top and hollow).^{30,33,104,105}

The MD simulations presented in this chapter revealed a third interfacial donor-acceptor geometry that I denoted by *edge* [see Figure 2.1(c)]. Previously, the *edge* geometry was not favorable when considered within a continuum dielectric model due to the smaller interfacial overlap between the donor and acceptor molecules. However, the *edge* geometry emerged in the explicit molecular treatment offered by my MD simulations, which revealed that the condensed-phase environment made it the dominant geometry in all five deposition models.

I found that, while the k^C value for the edge geometry was much lower than that of the *on-top* geometry, the higher population of *edge* still allowed it to play a significant role in determining device performance. Such a correlation between interfacial geometry and CT rates is likely not unique for the SubPC/C₆₀ system and is expected to play a role in other OPV systems.¹⁰⁶⁻¹⁰⁸

Charge separation in OPV systems follows a sequence of steps that determines the overall efficiency. These steps include charge diffusion,^{4,5,11,96,107} dissociation,^{29,108,109} and recombination,^{5,11,109-111} which are associated with a wide range of length and time scales.^{9,11,105-108,110,112-114} There appears to be evidence that interfacial CT plays a central role in determining the overall device performance and particularly in SubPC/C₆₀ systems.^{8,23,97} In this chapter, I focused on the interfacial CT step in a widely studied system, where to better understand the link between structural aspects, including that of the interface and device performance, future work will have to address the other steps and extend the analysis to the mesoscopic level. Essentially, all of the rates

of each step have to be determined to extract the cell parameters without imposing any assumptions.^{14,15}

My simulations addressed extreme cases of stacked layers. In particular, models I and II increased the occurrence of *on-top* and *hollow* interfacial pairs, respectively. Indeed, while in all cases the *edge* population was most dominant (between 70% and 80%), I found that over 10% of all pairs in model I were *on-top* pairs whereas in model II the *on-top* fraction drops to 2% and the *hollow*-pair fraction rises to close to 30%. Consequently, I found that the CT rate density was the largest for model I at 170 nA/nm² due to the increased share of the on-top pairs, whereas the other charge densities, including that of model II, were up to around 80 nA/nm². This appears to provide a good explanation of the measured trend of the short-circuit current, which is found to be strongly dependent on the order of layer deposition.⁸ Further studies are required to directly link the fabrication to the actual distribution of the interfacial pairs affected in the device measurements.

Charge-transfer states are strongly affected by the electrostatic environment, where they can be significantly stabilized to be lower than the absorbing-state energies.¹¹⁵⁻¹¹⁷ Therefore, such environmental effects are expected to greatly affect the charge-transfer rates. In this study, we used gas-phase-based electronic structure parameters, where the effects of the environment are captured through the MD simulations. The environmental electrostatic effects stabilized the CT states. I also note that recent efforts found that polarization effects addressed by a recently developed polarizable force field yield rates that reproduce the corresponding values achieved using a nonpolarizable force field.³⁴ While these observations were based on a solvated molecular triad, I also expect to find similar trends, where the polarization terms are only of a secondary effect, when considering OPV-related systems, as in this study. In addition, the recently developed screened

range-separated (SRSH) functional,⁷² which efficiently obtains environment-affected CT states,⁷⁷ has been used in the study of another OPV fullerene-based system³¹ and is used in Chapter 4.

E. Conclusions

I studied the interfacial D-A pairs in SubPC/C₆₀ OPV systems, and the associated CT across these pairs. I employed a comprehensive computational framework combining large-scale MD simulations, state-of-the-art quantum chemistry calculations, and the advanced rate theory of photoinduced CT. Large-scale MD simulations were employed to characterize the interfacial D-A pairs.

I found three categories of pairs, including *on-top*, *hollow*, and *edge*. The *edge* conformation, which had not been addressed in previous studies, was found to dominate the interface. However, the *on top* geometry, which comprised a significantly smaller portion of the interface, was found to have comparable CT rates to the hollow geometry in studies utilizing a polarizable continuum. The molecular resolution invoked here to study the kinetics identified it as promoting the CT process most effectively. This interplay of rate constants and conformational density highlights the scope for improving the ability of controlling the fabrication at the molecular level. I predict that increasing the relative weight of *on-top* conformational pairs achieves enhanced CT kinetics across the interface.

CHAPTER 3. CTRAMER: AUTOMATING THE ANALYSIS OF CHARGE TRANSFER

Adapted from: Tinnin J, *et al.* CTRAMER: An open-source software package for correlating interfacial charge transfer rate constants with donor/acceptor geometries in organic photovoltaic materials. *The Journal of Chemical Physics* **154**, 214108 (2021).

A. Introduction

In this chapter, I introduce a new software package, CTRAMER (Charge Transfer **R**ates from **M**olecular dynamics, **E**lectronic structure, and **R**ate theory), that provides computational tools for correlating interfacial CT rates with the underlying interfacial structure. The approach, which has been benchmarked and employed by my collaborators and I in previous work,^{3,92} combines state-of-the-art electronic structure calculations and molecular dynamics (MD) simulations to compute representative interfacial D/A geometries and the corresponding CT rate constants. The CT rate constants are calculated within the framework of Fermi's golden rule (FGR) and based on the linearized semiclassical (LSC) approximation.^{85,86,90,92-95} Support for other levels of CT theory is planned to be added in future versions. Each of the methods used in CTRAMER have been chosen due to being well-studied and performing well in benchmarks. It is the combination of these state-of-the-art methods from different fields that makes CTRAMER unique.

It should be noted that the FGR/LSC framework currently used for calculating CT rate constants in CTRAMER is based on treating the environment of the D/A pair at the molecular level, as opposed to treating it as a polarizable continuum or a harmonic bath.^{3,86} Such resolution is required to account for the heterogeneity of the solid state environment and the distribution of D/A geometries and CT rates it can give rise to.^{3,19,75,85,96,118-120} It should also be noted that the molecular

models I use are parameterized based on inputs obtained from *ab initio* electronic structure calculations.

My primary goal in this chapter is to introduce a general-purpose software package based on the computational framework outlined above, summarize the available features in it, and demonstrate its applicability and scope by presenting results from an example OPV system where boron subphthalocyanine (SubPC) serves as the donor and fullerene (C_{60}) serves as the acceptor.^{4,6,8,14,23-28,33} This framework could be broadly applied to other materials.

B. CTRAMER methodology

The overall workflow for CTRAMER is outlined in Figure 3.1. The algorithm is initiated by the molecular coordinates of the donor and acceptor [Figure 3.1(a)]. The output corresponds to CT rate constants for different interfacial D/A geometries, which can be used to correlate the interfacial CT rate constants to the interfacial structure.

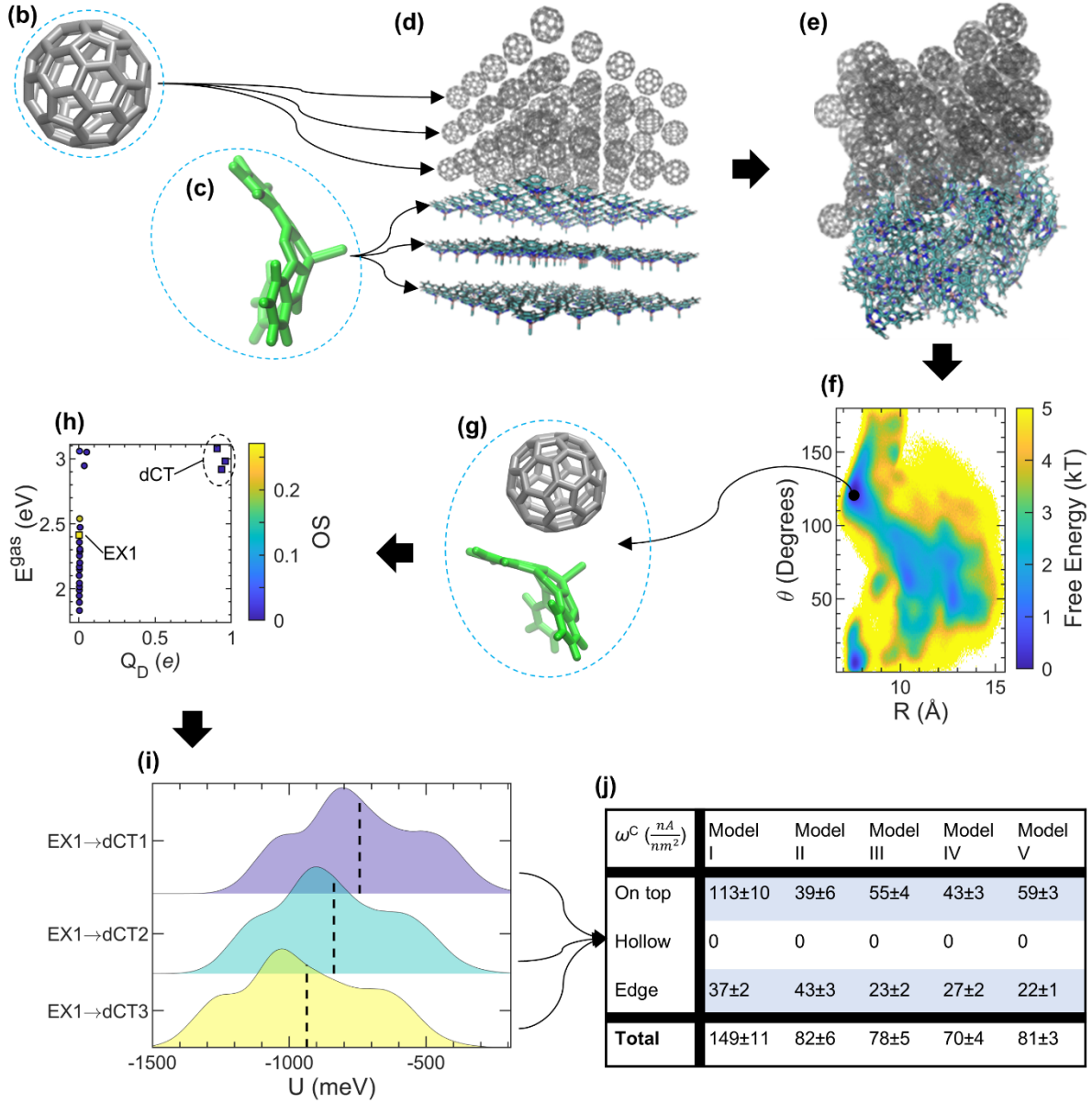


Figure 3.1. The overall workflow for CTRAMER (illustrated on the SubPC/ C_{60} system). (a)/(b) correspond to the C_{60} /SubPC molecules respectively, where the blue dashed enclosures represent electronic-structure calculations done for each molecule separately. (c) A condensed-phase system constructed using the molecular coordinates from (a) and (b) as well as the Mulliken charges obtained therein. (d) An equilibrated snapshot of the (c) system after equilibration. (e) The potential of mean force for the system in (d), where a coordinate in (R, θ) space corresponds to a SubPC/ C_{60} pair. (f) A SubPC/ C_{60} pair selected from (e), the blue dashed enclosure representing electronic-structure calculations done on the pair. (g) Scatterplot of characteristics for excited states calculated in (f). (h) Distribution of fluctuations in the energy gap of transitions between states selected from those calculated in (f). (i) Charge-transfer rate-constant densities for the configuration from (f)-(h) (in this case, hollow) as well as two others. The numbers for each model vary according to the population of each configuration.

i. Softwarization flow

CTRAMER consists of five modules as shown in Figure 3.2. The modules address the different scales needed for describing the CT process occurring at a D/A core that is affected by its molecular environment. The modular nature of CTRAMER allows the user to exclude or replace steps as needed. To initiate the calculation, the individual donor and acceptor molecules' [see Figure 3.1(a) and 3.1(b)] atomic coordinates are obtained from literature or experiment. In Module 1, the atomic charges of the donor and acceptor molecules are calculated using density functional theory or assigned using published force-fields. Module 2 combines multiple donor and acceptor molecules [Figure 3.1(c)] and equilibrates the overall system using the charges from Module 1 to a pre-assigned temperature and pressure [Figure 3.1(d)]. This is followed by a determination of the distribution of interfacial D/A pair geometries in a form of multiple parallel trajectories [Figure 3.1(e)]. Module 3 performs electronic state calculations on selected representative interfacial D/A pairs that correspond to different classes of geometries [Figure 3.1(f)]. From these calculations, excited donor and acceptor states are identified using a preset criteria of excited states properties (oscillator strength and CT characteristics) [Figure 3.1(g)]. Here the relevant transitions and the coupling between the donor and acceptor states are obtained. Module 4 uses MD simulations to calculate the fluctuations in the D/A energy gap in the condensed phase [Figure 3.1(h)]. Combining these fluctuations with CT characteristics from Module 3, LSC-based E-FGR CT rates [Figure 3.1(i)] are obtained by Module 5 at the chosen level of theory.

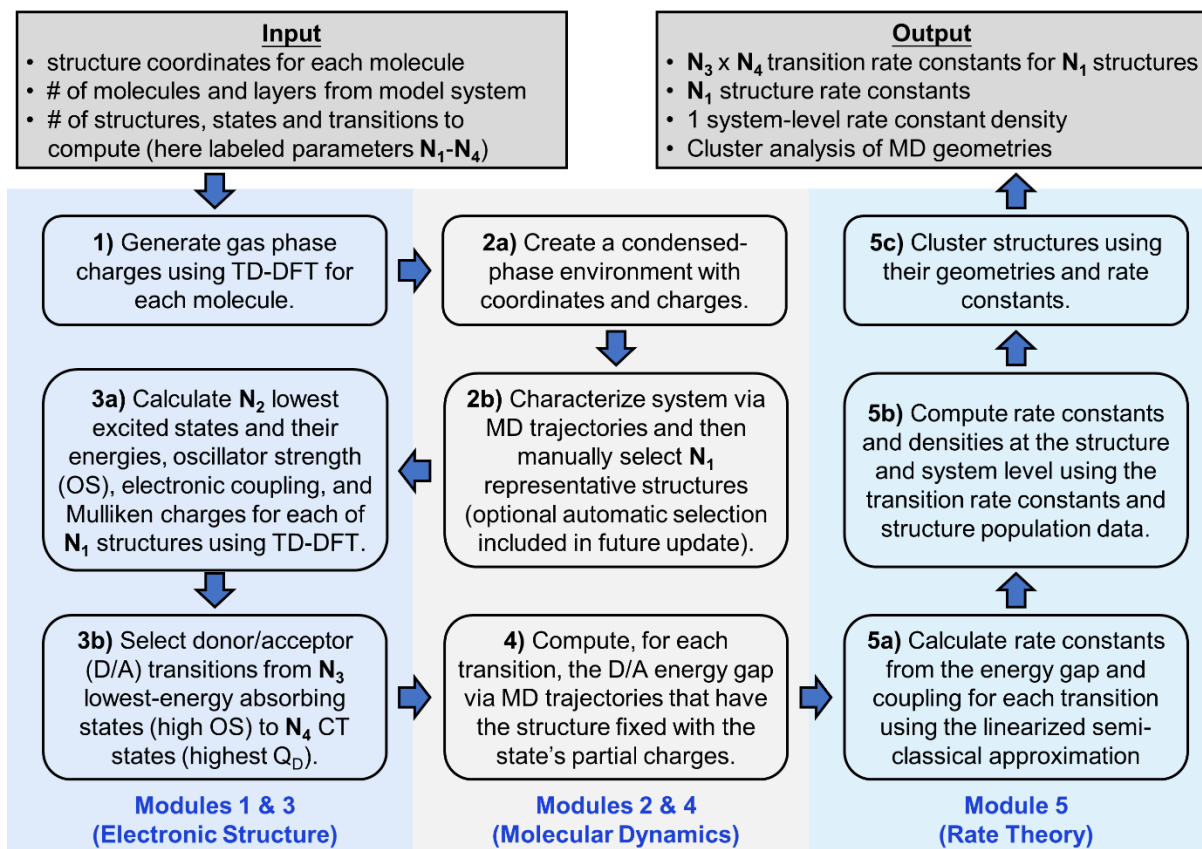


Figure 3.2. Flowchart representing information flow during each section of the software. Each box represents a process while the arrows represent data within the software. Input parameters are the number of representative structures from MD (N_1), excited states from Q-Chem (N_2), and excitonic (N_3) / CT (N_4) states for which transitions are selected.

ii. Computational Approach

Figure 3.3 illustrates the actual scripts that comprise each module in CTRAMER. The electronic structure calculations and the MD simulations reported in this manuscript are based on Q-Chem 4.0⁵² and AMBER12³⁷ respectively. All the scripts are available on GitHub¹²¹ (<https://github.com/ctramer/ctramer>). Below, I provide additional information on the procedures for establishing the different parameters under each module.

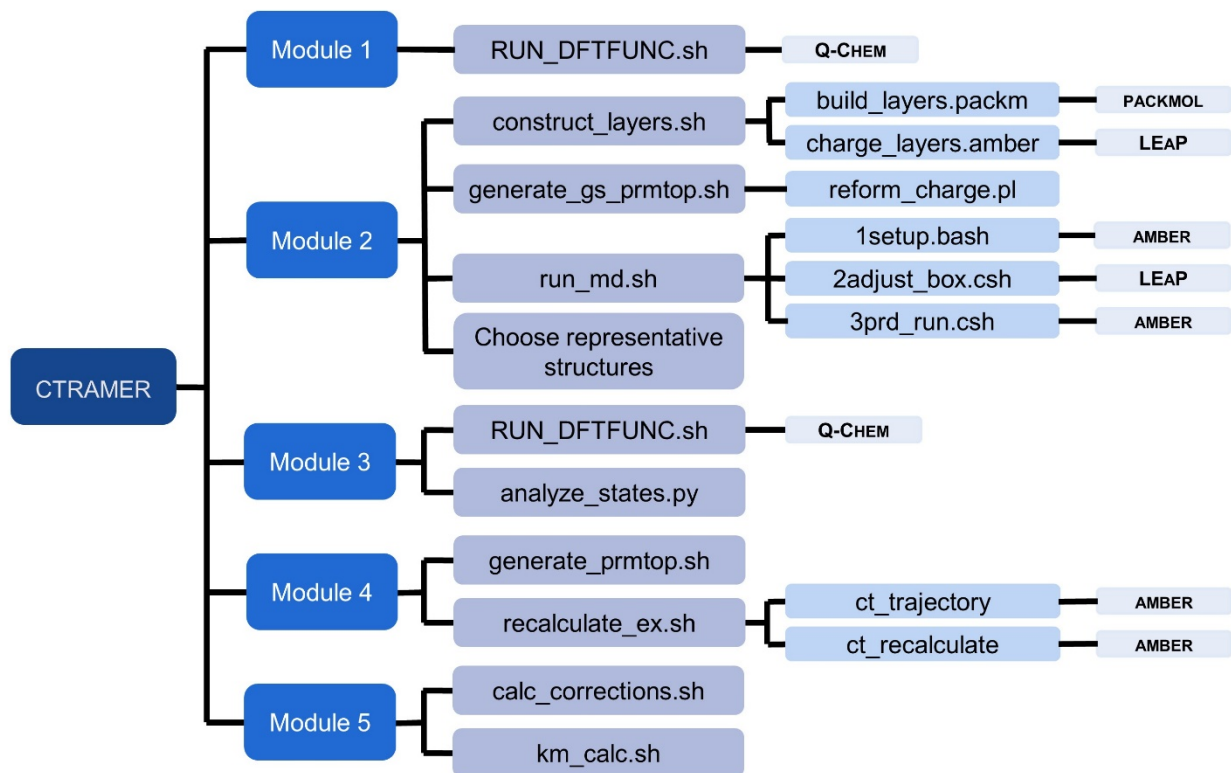


Figure 3.3. Execution of the CTRAMER scripts in order. (available on Github: <https://github.com/ctramer/ctramer>)

iii. Electronic structure calculations (Modules 1 and 3)

Time-dependent density-functional theory (TD-DFT) calculations are used in two modules of CTRAMER. First, in Module 1, TD-DFT is used on individual molecules to obtain partial charges for use in the MD simulations of Module 2. In Module 3, TD-DFT is used on selected interfacial D/A molecule pairs to obtain excited states and their partial charges, oscillator strength (OS), and relative energy.⁵³ These electronic structure protocols are benchmarked against experimental measured excitation energies⁷⁵⁻⁷⁷ (including those of charge transfer states) as well as measured rates.^{4,78} I note that, in the condensed phase, as molecules tend to neighbor several molecules, each molecule can be involved in multiple D/A pairs. I hypothesize that, on the macroscopical scale, CT follows the paths involving the D/A pairs with the fastest rate constants on the microscopical scale.

Important excited states are selected and then classified as donor and/or acceptor states. CTRAMER calculates the electronic coupling coefficients between electronic states using the fragment-charge-differences (FCD) method.⁸⁰ Choice of functional and basis set can be customized for the system under study based on literature and experimentation.

For the results presented in this chapter, I used the 6-31G* basis set¹⁰³ and Baer-Neuhauser-Livshits (BNL) range-separated hybrid functional^{167,68} for TDDFT calculations. A γ value of 0.167 bohr⁻¹, tuned to an optimal value for the *on-top* geometry based on the J2(γ) scheme⁶⁹, was used for all the geometries.

Calculated excited states are classified as follows. First, the charge of the donor molecule, Q_D , is used to classify states either as non-CT ($Q_D < 0.25 e$) or CT ($Q_D > 0.25 e$). Second, states with a significant OS are referred to as light-absorbing states, or *bright*.⁷⁹ CT states with negligible OS are referred to as *dark* (dCT) and those with a significant OS are addressed as bright CT (bCT).

Non-CT states with significant OS are referred to as excitonic (EX). As CTRAMER studies direct CT from photoexcited (bright) states to CT states, states that are both dark and non-CT are not addressed. However, extensions to consider additional processes can be developed in future versions. The states are then named as EX n , bCT n , or dCT n . The index n refers to the rank of a state's energy, from smallest to largest, within EX, bCT, and dCT states with the same geometry. Classification thresholds can be customized within CTRAMER.

Last, using these classified states, transitions from a bright state to a CT state are selected. The user selects the maximum number of donor and acceptor states between which transition rates are calculated. The computational cost is linear with the number of donor states but is largely unaffected by the number of acceptor states (as MD is performed only on the donor state as detailed in Chapter 3.B.v). As part of these electronic structure calculations, electronic coupling coefficients are computed for each transition.

iv. Molecular dynamics simulations (Modules 2 and 4)

Module 2 focuses on creating a condensed-phase system from the coordinates and charges established in Module 1, equilibrating it to a given temperature and pressure, and then analyzing the distribution of structures. From this distribution, representative structures are selected for further analysis along with their surrounding molecules. In simulations during Module 4, an interfacial molecular pair is kept fixed for use in calculating energy gaps between excited states. These energy gaps are used in Module 5 to calculate rate constants.

CTRAMER uses Packmol⁹⁸ to construct condensed-phase OPV systems. Packmol places a user-defined number of molecules into a region of space, the size of which is also set by the user. CTRAMER by default uses 6 square layers into each of which it places 25 molecules. Each layer

consisted of only one type of molecule. Space is placed between separate types of layers to simulate the fabrication procedure. Too much or too little space between molecules can cause the system to not equilibrate correctly.

The MD simulations of CTRAMER utilize the generalized AMBER force field (GAFF),³⁵⁻³⁷ augmented by other force fields (FFs) as needed. For example, interactions involving the boron atom that is found at the center of SubPC are not given in GAFF and were here taken from Refs. 99,100 (see Table 2.1). The MD simulations are performed by the AMBER12 program SANDER.³⁷ CTRAMER fits the simulation box to the constructed system and then applies periodic boundary conditions. Both equilibration and production MD simulations have a time step of 2.0 fs. The SHAKE algorithm³⁹ is used to constrain bonds involving hydrogen. Neighbor list updates, real-space Coulomb interactions, and van der Waals interactions utilize a 10.0 Å threshold. CTRAMER calculates electrostatic interactions with the particle-mesh Ewald method.^{40,41}

By default, a hybrid algorithm is used to perform energy minimization. The default settings for this algorithm, used for the results in this chapter, are listed here. The conjugated-gradient method is used for 500 timesteps, followed by 4500 timesteps of the steepest-descent method. The minimized system is then heated to 298.15K using the canonical ensemble (NVT) gradually over a period of 10 ps. CTRAMER then fixes the system at this temperature for 1.0 ns and equilibrates at a constant pressure of 1.0 bar using a NPT ensemble with 1.0 ps as the pressure relaxation time. The simulation box is then refit to the equilibrated system with periodic boundary conditions kept. A planned future update is for CTRAMER to simulate automatically until equilibration is reached.

Production runs in Module 2 use the equilibrated system with the adjusted box size in a NVT ensemble. As with all other parameters, the number and length of production runs can be

specified by the user. For the results shown in this chapter, one run of 20 ns was used. In my tests on CTRAMER, multiple production runs can aid in sampling multiple local minima.

Productions run in Module 4 use the entire system in the timestep in Module 2 from which a representative geometry was chosen. The atoms of the representative pair are fixed in place using a harmonic potential. By default, CTRAMER uses a force constant of 50 kcal/mol-Å². However, as the energies calculated by CTRAMER do not include the restraint potential, the size of the force constant will not affect the results.^{34,37} The goal of fixing the atoms is to keep the molecules in the representative geometry. These fixed atoms are assigned with Mulliken partial charges, from Module 3, of a donor state for that representative pair geometry. The rest of the molecules in the system have ground state charges from Module 1 and are unrestrained. After equilibration, production runs are performed using the same parameters as Module 2. The effect on uncertainty in rate constants in Module 5 by changing the number and length of production runs in Module 4 is discussed in Chapter 3.B.v.

v. Rate evaluations (Module 5)

Module 5 can evaluate CT rates at different levels. Below, I show how to calculate transition rate constants following a Marcus-level linearized semi-classical (LSC)^{3,86,92,93} approximation to Fermi's Golden Rule, where the donor-to-acceptor transition rate constant (k^M) is given by:

$$k^M = \frac{|V_{DA}|^2}{\hbar} \sqrt{\frac{2\pi}{\sigma_U^2}} \exp\left[-\frac{\langle U \rangle^2}{2\sigma_U^2}\right]. \quad (3.1)$$

Here, $U(\mathbf{R}) = V_D(\mathbf{R}) - V_A(\mathbf{R})$ is the D/A energy gap as a function of the nuclear coordinates, \mathbf{R} , where V_D and V_A are the potential-energy surfaces of the donor and acceptor states, respectively. $\langle U \rangle$ and σ_U are the first and second moments, respectively, of $U(\mathbf{R})$. This rate

constant was derived from Fermi’s Golden Rule by the LSC approximation, as detailed in refs. ^{86,92,94,95}, but is referred to as “Marcus-level” as the reorganization energy, E_r , the reaction free energy, ΔE , and the activation energy, E_a , can be calculated from $\langle U \rangle$ and σ_U : $E_r = \sigma_U^2 / (2k_B T)$, $\Delta E = -E_r - \langle U \rangle$, and $E_a = k_B T \langle U \rangle^2 / (2\sigma_U^2)$. These parameters allow for the analysis of rates calculated using Marcus Theory.⁸¹⁻⁸⁴ The electronic excitation energies are from the Module 3 electronic structure calculations.

$U(\mathbf{R})$ is determined for each transition using classically sampled trajectories of a D/A pair fixed in place with donor state charges as detailed in Chapter 3.B.iv. Then, the potential energy surface at a given timestep in a trajectory, V_α^M , is calculated for each state, with α denoting the donor or the acceptor, by recalculating the energy of the entire system in AMBER12.³⁷ To avoid double counting of potential energy by the electronic structure and MD methods, V_α^M is corrected to $V_\alpha = V_\alpha^M + W_\alpha$, where W_α is the difference in single-point energy of each state between calculations by the electronic structure and MD methods. U is then determined using the difference of V_D and V_A . Finally, $\langle U \rangle$ and σ_U are obtained using the moments of N_R MD trajectories of length L_R . I here used $N_R=40$ runs and $L_R=40$ ns, which can be adjusted for the desired accuracy. The uncertainty for rate constants decreases approximately as $\frac{1}{\sqrt{N_R L_R}}$.

As shown in Figure 1.5 and Figure 3.1(h), the distribution of $U(\mathbf{R})$ can be significantly non-Gaussian for many transitions. I attribute this to CTRAMER accounting for how the condensed phase’s heterogeneity can lead to multiple local energy minima. As the LSC approximation uses a Gaussian distribution to model the probability density at $U(\mathbf{R}) = 0$, CTRAMER resolves these energy minima by best fitting the probability density function of $U(\mathbf{R})$ to a sum of Gaussian distributions chosen by least-squares regression. CTRAMER increases the number of distributions,

beginning at one, until the 95% confidence interval for σ_U includes non-positive numbers or a maximum of three is reached. These settings can be customized within CTRAMER.

While k^M measures the transition rate between states, I multiply it by the amount of the corresponding charge transferred, (ΔQ_D), to measure the rate of CT (k^C) for a transition:

$$k^C = \Delta Q_D k^M. \quad (3.2)$$

Both k^C and k^M are obtained in the context of a single transition for one structure. For aid in comparison between structures, these CT rates are summed over all the identified transitions, t , for a given representative structure i , to give a structure-level CT rate constant (K_i^C):

$$K_i^C = \sum_t k_t^C. \quad (3.3)$$

A system-level CT density (ω^C) can then established by averaging K^C over the area of the D/A interface in the simulation:

$$\omega^C = \sum_i (K_i^C n_i) \times \frac{1}{A}, \quad (3.4)$$

where n_i is the number of pairs represented by the structure i from Equation 3.3 and A is the approximate area of the interface (which is by default calculated by CTRAMER but can be replaced).

C. Results

CTRAMER was used to analyze the CT rate in the interface of SubPC/C₆₀ pair of donor acceptor organic material used in model OPV studies. CTRAMER can be used for many materials, but these results are presented here as an example use of the software. Data is available at <https://github.com/ctramer/ctramer>.¹²¹

i. Sample preparation (Module 1)

The coordinates of the optimized SubPC and C₆₀ molecules are provided on GitHub¹²¹ (<https://github.com/ctrimer/ctrimer>), while the references used to determine the atomic charges are listed in Table 2.1.

ii. Condensed-phase structures (Module 2)

The multilayered OPV system was represented using 6 alternating layers of 25 SubPC or C₆₀ molecules each. A large ensemble of interfacial D/A pairs was then obtained, where a interfacial D/A pair was defined as 1 SubPC molecule and 1 C₆₀ molecule where the minimum distance between any atom from separate molecules was less than 5 Å.

Analysis of the different interfacial pairs was aided by two order parameters [see Figure 3.4(b)]: first, the distance (R) between the SubPC boron atom and the C₆₀ center of mass, and second, the angle (θ) between the vector from the C₆₀ center of mass to the SubPC boron atom and the vector from the SubPC boron atom to the SubPC chlorine atom.

Inspection of the potential of mean force (PMF) using a (R, θ) coordinate system [shown in Figure 3.4(a)] reveals two pronounced regions of low energy centered at approximately (7.5 Å, 0°) and (7.5 Å, 120°), which correspond to D/A pair geometries identified as *on top* and *hollow* in previous gas-phase and mean-field studies^{3,4,23,69,122} [examples of which are shown in Figure 3.4(a)]. The approximate percentage of sampled D/A pairs corresponding to these geometries [shown in Figure 3.4(a)] were calculated using D/A pairs where $R < 8.5$ Å and $\theta < 38^\circ$ for *on top* and D/A pairs where $R < 9$ Å and $95^\circ < \theta < 160^\circ$ for *hollow*.

However, the majority of the D/A pairs in the PMF did not correspond to either *on top* or *hollow*. Instead, these pairs corresponded to a geometry, noted as *edge*, that was identified using

the condensed-phase analysis in Chapter 2.³ While most of the *edge* pairs fell within the range of $10 \text{ \AA} < R < 14 \text{ \AA}$ and $40^\circ < \theta < 100^\circ$, they had a large variance in R and θ [one example structure is shown in Figure 3.4(a)]. The *edge* geometry consisted of pairs where only the *edge* of a SubPC arm was close to the C_{60} molecule. Most of the *edge* pairs fell within the following range on the PMF: $10 \text{ \AA} < R < 14 \text{ \AA}$ and $40^\circ < \theta < 100^\circ$.

Among the ensemble structures from each basin (e.g. *on-top*, *hollow*, or *edge* ensembles), the most probable structure was selected as the representative D/A pair geometry for analysis in Module 3.

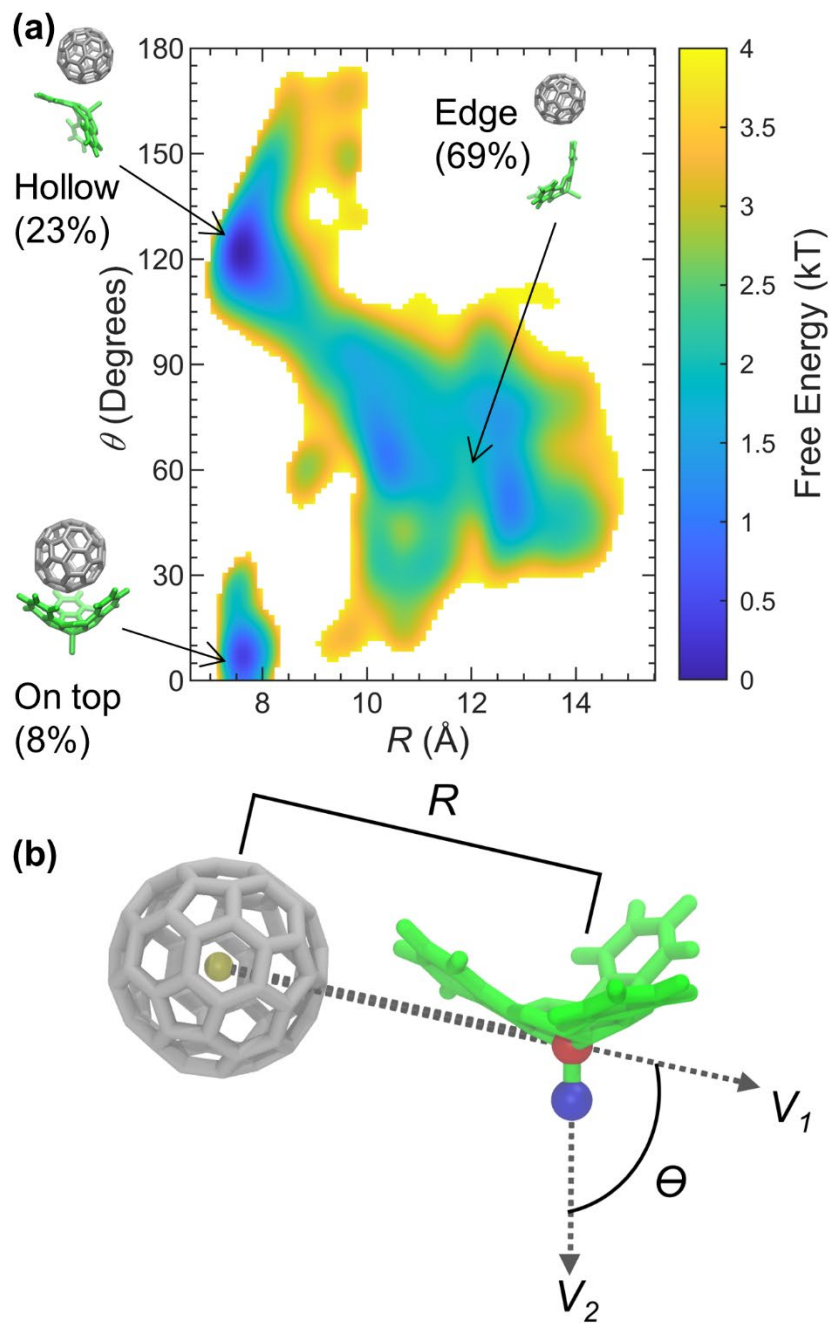


Figure 3.4. The potential of mean force (a) for the SubPC/C₆₀ pair on a R - θ coordinate system. The color is scaled by $k_B T$. Also shown are representative structures (*on top*, *hollow*, and *edge*) of SubPC/C₆₀ pair at each of the three major geometries and the percentage of interfacial pairs in that geometry. R and θ are defined in (b), where the yellow bead corresponds to the C₆₀ center of mass and the red and blue beads correspond to the SubPC boron and SubPC chlorine atoms, respectively. R is the distance between the SubPC boron atom and the C₆₀ center of mass. θ is the angle between vectors V_1 and V_2 .

iii. Electronic structure results (Module 3)

Electronic structure calculations were performed on the interfacial D/A geometries selected from Module 2. The important parameters are (1) the charge of the D/A pair's donor molecule (Q_D), (2) the energy for the D/A pair while isolated in the gas-phase (E^{gas}), and (3) the pair's oscillator strength (OS).⁷⁹ These three parameters are shown by the x axis, y axis, and color bar, respectively, in Figure 3.5.

Transitions studied here are from the lowest-energy bright EX state to each of the dark CT states, with one exception: in the *on-top* geometry, a bright CT state was considered as a donor state in addition to the lowest-energy EX state and also as an acceptor state. The OS of the bright states for the *on-top* geometry was about half that of the EX1 state for the *hollow* and *edge* geometries, as shown in Figure 3.5 and listed in Table 2.4. *Hollow* and *edge* each also had another EX state that is similar in both OS and E^{gas} but was not used for these results. However, the dCT states for *on top* ranged from approximately equal to slightly lower in energy than its bright states while all the dCT states for *hollow* and *edge* were much higher in energy than the bright states. The exact values shown in Figure 3.5 were recorded in Table 2.4. EX and CT states as labeled in Figure 3.5 were used for analysis in Module 4.

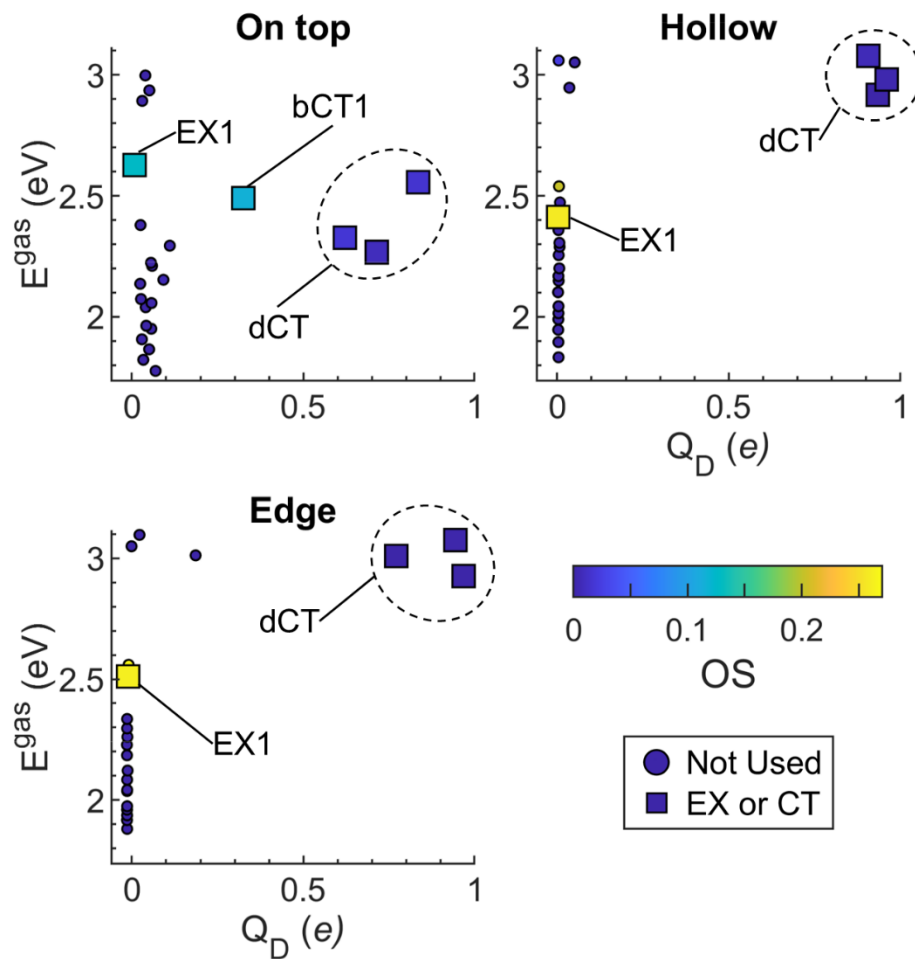


Figure 3.5. Excited state properties for the three SubPC/ C_{60} representative pair geometries. A scatter plot is shown of the excitation energy in the gas phase (E^{gas}) versus the charge of the donor molecule (Q_D) for each geometry. Dots are colored according to their oscillator strength (OS). States used for calculations in this chapter are shown by large squares and labelled while other states are denoted by smaller circles. The 25 lowest-energy excited states are shown for each geometry.

iv. Charge-transfer rate constants (Modules 4 and 5)

Next, I calculated the electronic-population-transfer rate constant, k^M , and CT rate constant, k^C , for transitions from a donor state (EX1 or bCT1) to an acceptor state (bCT1, dCT1, dCT2, or dCT3). The required inputs to calculate k^M , as shown in Equation 3.1, were the D/A energy-gap first and second moments, the coupling coefficient, Γ_{DA} , and the excitation-energy correction, W_α , (see Figure 3.6, Table 3.1, and Table 2.2). The relative energies between states were changed in MD simulations due to the molecular environment. Clearly, the CT states were expected to be stabilized by the condensed-phase polarizable environment more than the localized excitations.⁹⁶ The rate constant, k^C , (see Table 3.1) was the product of k^M and ΔQ_D , the difference in charge of the donor molecule between the donor and acceptor states.

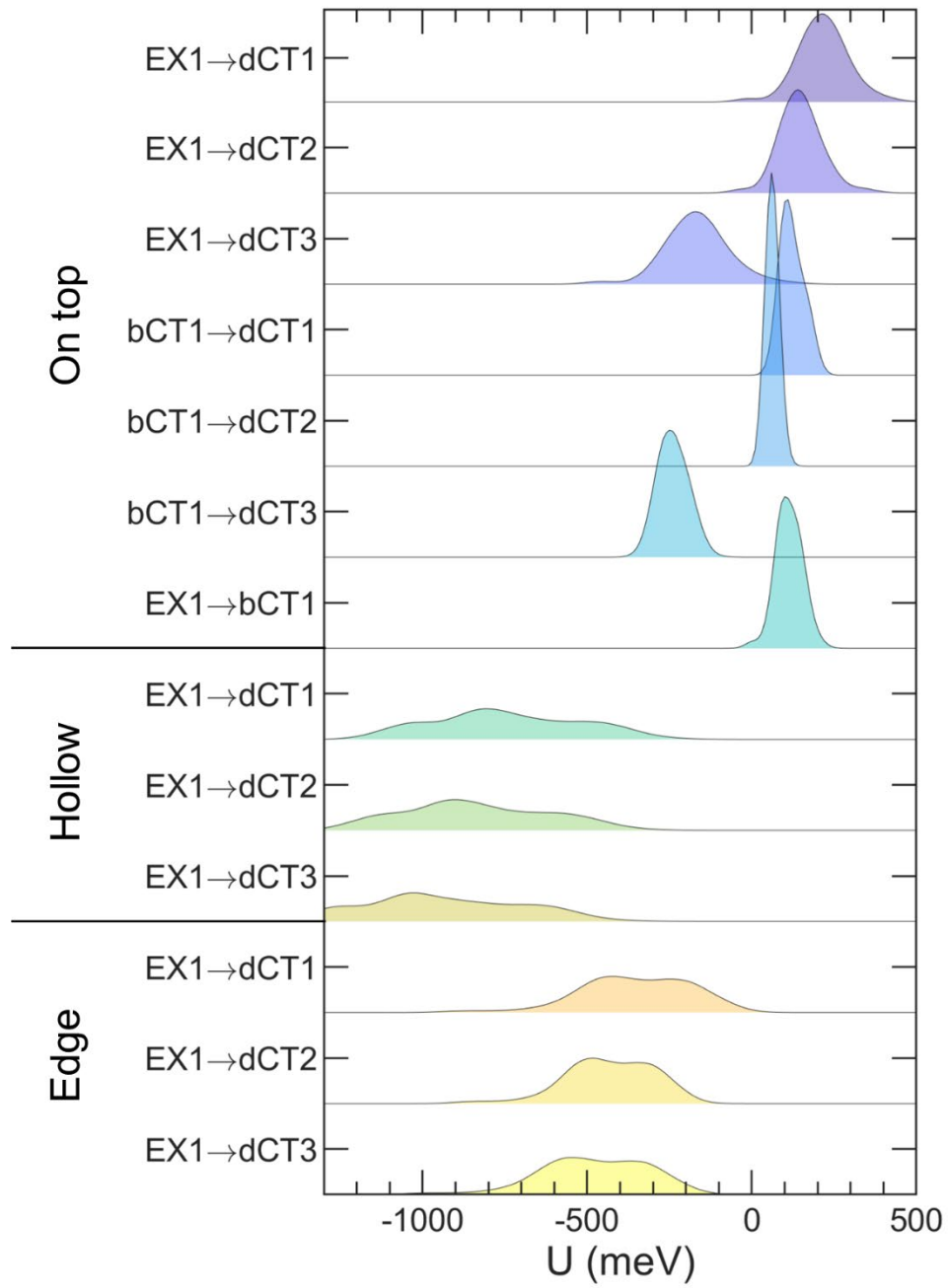


Figure 3.6. A ridgeline plot of the probability density functions of $U(\mathbf{R})$.

In the *on-top* geometry, the Γ_{DA} for the bCT1 \rightarrow dCT1 and bCT1 \rightarrow dCT2 transitions were at least double the size of any other Γ_{DA} considered. On the other hand, as transitions involving bCT1 used a CT state as donor state, ΔQ_{D} for these transitions was significantly less than that of transitions with an EX donor state. As a result, the values of k^{C} for transitions with either EX1 or bCT1 as the donor state in the *on-top* geometry were within an order of magnitude of each other. Additionally, the values of k^{M} were comparable to those from a non-condensed-phase analysis based on optimized geometries.⁴

For both the *hollow* and *edge* geometries, smaller Γ_{DA} values for transitions from EX1 to dCT states than those in the *on-top* geometry led to smaller rate constants. However, the k^{C} values for the *edge* geometry were larger overall than those of the *hollow* geometry. This difference between *edge* and *hollow* can be traced back to the fact that the transitions in the edge geometry corresponded to a much smaller $\langle U \rangle$ than those of the hollow geometry (see Table 3.1). The k^{M} values for transitions in the *hollow* geometry were observed to be significantly smaller than those previously reported in a non-condensed-phase analysis based on optimized geometries (see Table 2.7).⁴ Marcus theory parameters are available for all transitions in Table 2.6.

Table 3.1. Interfacial charge-transfer rates for the three SubPC/C₆₀ representative pair geometries

Geometry	Transition	Γ_{DA} (meV)	ΔQ_D (e)	$\langle U \rangle$ (meV)	k^C (nA)
<i>On top</i>	EX1→dCT1	4.03	0.706	217±2	180±10
	EX1→dCT2	24.46	0.616	148±11	520±70
	EX1→dCT3	5.47	0.825	-168±1	220±10
	EX1→bCT1	25.82	0.314	114±5	510±40
	bCT1→dCT1	74.16	0.391	123±2	24±2
	bCT1→dCT2	72.27	0.302	61.6±0.1	1,010±20
	bCT1→dCT3	21.13	0.511	-240±12	0.014±0.008
<i>Hollow</i>	EX1→dCT1	1.85	0.943	-743±14	0.006±0.002
	EX1→dCT2	20.21	0.959	-837±14	0.04±0.02
	EX1→dCT3	15.53	0.905	-936±30	0.006±0.004
<i>Edge</i>	EX1→dCT1	10.30	0.977	-354±23	65±5
	EX1→dCT2	14.02	0.781	-432±15	0.32±0.07
	EX1→dCT3	17.22	0.953	-481±20	3.1±0.6

D. Conclusions

I have described the software package CTRAMER for the analysis of CT rates based on electronic structure calculations, MD simulations, and rate theory. CTRAMER is a unique combination of well-established methods from different disciplines that allows for a more precise study of photoinduced CT between excited states and explicit environment. The customizable features, software architecture, and guidelines for usage were discussed. Additionally, the scientific justification behind the different approaches as well as example results were described.

CTRAMER will continue to be actively developed and supported, as it will remain a long-term focus of the authors. Additions planned for the immediate future are automated tuning of the parameters for electronic structure calculations, enabling different level of theory, and machine-learning clustering methods for selecting representative structures. Other future goals include various extensions to improve the accessibility and computational efficiency of the software.

CHAPTER 4. MOLECULAR ANALYSIS OF DBP/C₇₀

CHARGE TRANSFER

A. Introduction

Herein, I study the correlation between molecular morphology and CT (shown in Figure 4.1) in an OPV cell consisting of Tetrphenyldibenzoperiflanthen (DBP), shown in Figure 4.2(a), as the electron donor and a fullerene (C₇₀), shown in Figure 4.2(b), as the electron acceptor. The DBP/C₇₀ cell is well-studied system with unique geometries and a complex electronic structure.^{31,32}

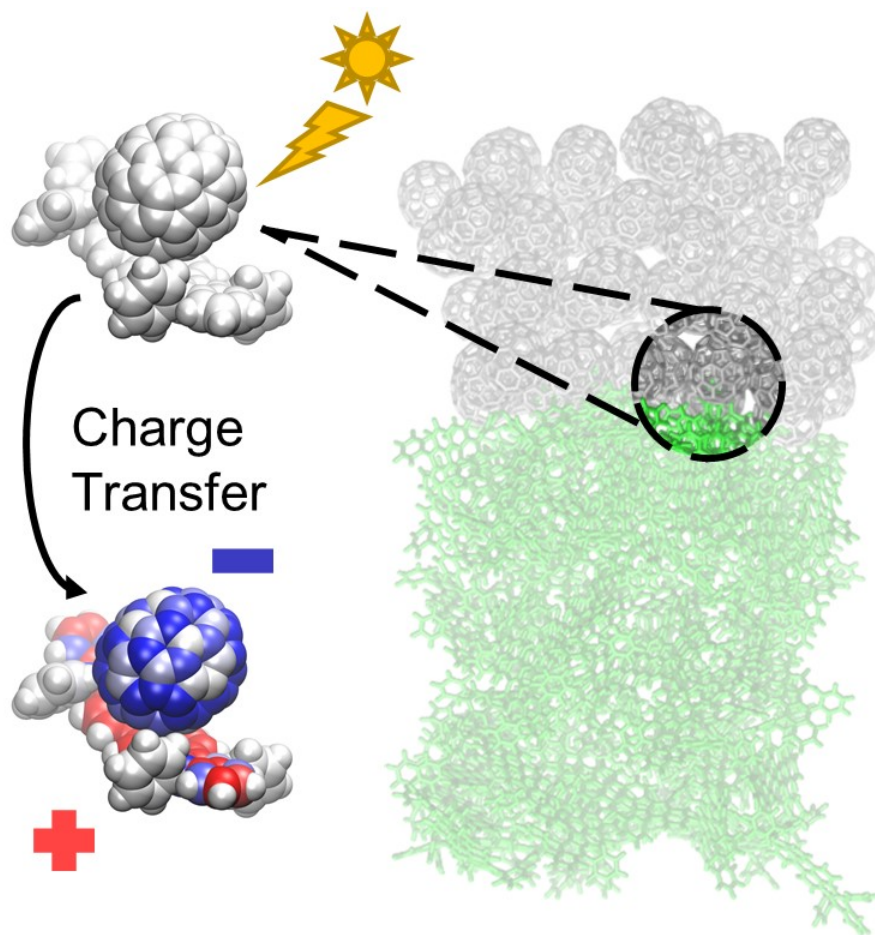


Figure 4.1. DBP/C₇₀ pairs are selected from an explicit condensed-phase environment to account for the effect of molecular morphology on charge transfer.

For this analysis, I utilize a recently introduced software package, CTRAMER¹⁶ (Charge Transfer RAtes from Molecular dynamics, Electronic structure, and Rate theory), which provides computational tools to correlate interfacial CT rates with the underlying interfacial structure. This approach, which has been benchmarked and employed by my collaborators and I in our previous work,^{3,92} combines state-of-the-art electronic structure calculations and molecular dynamics (MD) simulations to compute representative interfacial D/A geometries and their corresponding CT rate constants. The CT rate constants are calculated within the framework of Fermi's golden rule (FGR) and based on the linearized semiclassical (LSC) approximation.^{85,86,90,92-95}

The FGR/LSC framework, used in this chapter for calculating CT rate constants, treats the environment of the D/A pair at the molecular level and not as a polarizable continuum or a harmonic bath.^{3,86} This level of resolution is required to account for the heterogeneity in the solid state environment as well as the distribution of D/A geometries and CT rates produced by this heterogeneity.^{3,19,75,85,96,118-120} Moreover, the molecular models used herein are parameterized based on inputs obtained from electronic structure calculations.

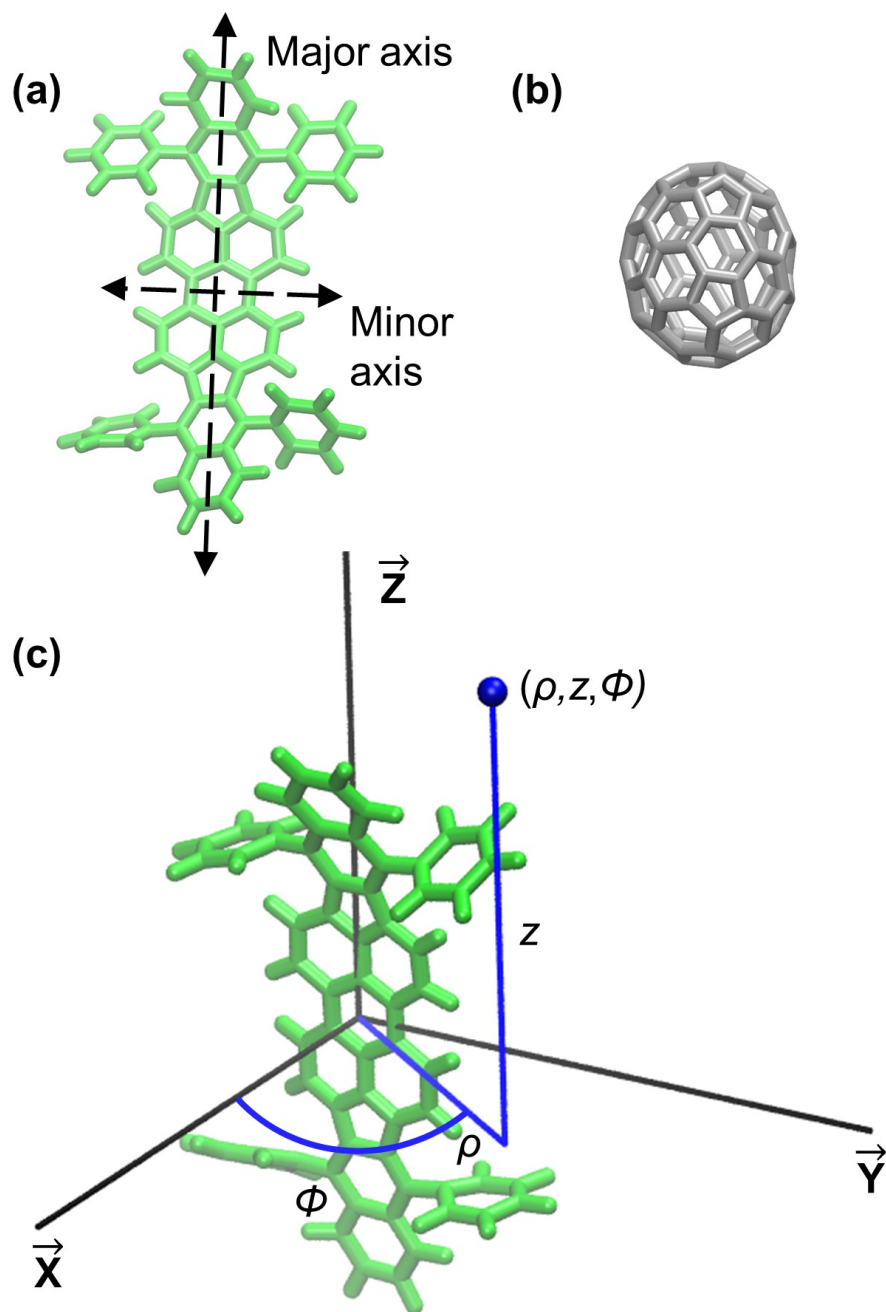


Figure 4.2. DBP (a) and C_{70} (b) molecules with the cylindrical coordinate system (c) used to define order parameters. Pairs are classified according to the center of mass of C_{70} being “on” ($[1]$) or “off” ($[0]$) the major and minor axes of DBP shown in (a).

B. Methods

Calculations in this chapter were done following the guidelines in Chapter 1. Adaptions specific to the results presented in this chapter are described in the following.

i. Electronic structure calculations

I used the 6-31G* basis set¹⁰³ and a screened-range-separated hybrid (SRSH) functional^{73-75,123} based on the PBE functional for TD-DFT calculations. An optimally tuned γ value^{67,68} of 0.155 bohr^{-1} , obtained for the $[I, I]$ geometry based on the $J2(\gamma)$ scheme⁶⁹, was used for all the geometries. A polarizable continuum method (PCM)^{124,125} was used to treat the area surrounding the molecular pair during electronic structure calculations. These electronic structure protocols have been benchmarked against experimentally measured excitation energies⁷⁵⁻⁷⁷ (including those of charge-transfer states) as well as measured rates.^{4,78} I note that, in the condensed phase, as molecules tend to neighbor several molecules, each molecule can be involved in multiple D/A pairs. I hypothesize that, at the device level, CT follows the paths involving the D/A pairs with the fastest pair-level CT rate constants.

Important excited states were selected and then classified as donor and/or acceptor states as follows. First, the charge of the donor molecule, Q_D , was used to classify states either as non-CT ($Q_D < 0.25 e$) or CT ($Q_D > 0.25 e$). Second, states with a significant OS were referred to as light-absorbing states, or *bright*.⁷⁹ CT states with negligible OS were referred to as *dark* (dCT) and those with a significant OS were addressed as bright CT (bCT). Non-CT states with significant OS were referred to as excitonic (EX). As this chapter studies direct CT from photoexcited (bright) states to CT states, states that are both dark and non-CT were not addressed. The states were then

named as EX n , bCT n , or dCT n . The index n referred to the rank of a state's energy, from smallest to largest, within EX, bCT, and dCT states with the same geometry.

ii. System preparation and molecular dynamics simulations for population analysis

Packmol⁹⁸ was used to construct the condensed-phase OPV systems of 6 square layers of 25 molecules each shown in Figure 1.2 and Figure 4.1. Each layer consisted of only one type of molecule. Space was placed between separate types of layers to simulate the fabrication procedure.

Production runs for population analysis were run on the equilibrated system (shown in Figure 1.2 and Figure 4.1) with the adjusted box size in a NVT ensemble. Six parallel runs of 5 ns each were used.

iii. Population analysis using energy landscape theory and physics-guided machine learning

DBP/ C_{70} pairs were sampled from the MD production runs where an interfacial D/A pair was defined as 1 DBP molecule and 1 C_{70} molecule where the minimum distance between any atom from separate molecules was less than 5 Å. The pairs were then characterized using a cylindrical coordinate system as shown in Figure 4.2(c) for the C_{70} center of mass with the origin at the DBP center of mass. To account for the symmetry of DBP, points are reflected such that $Z \in [0 \text{ Å}, \infty \text{ Å})$ and $\Phi \in [0^\circ, 90^\circ]$.

The Z - Φ probability density is then estimated using 2D kernel density estimation.^{42,43} The bandwidth is optimized⁴⁴ individually for each variable to minimize L2 loss, or mean integrated squared error. The density at the boundaries of support is corrected using the reflection method.⁴⁵ From this density estimate, the free energy is calculated using the Boltzmann approximation. Ridgelines between free energy basins are determined by finding neighboring grid points of

highest energy beginning from a point on the edge of bounded support. Representative geometries were chosen from the local energy minima within the region.

iv. Molecular dynamics simulations for rate calculations

Production runs for rate calculations used the entire system in the timestep from which a representative geometry was chosen. Five parallel production runs of 5 ns were used for each transition with 5 ns of equilibration for each run.

v. Rate calculations using the linearized semi-classical approximation

While k^M measures the transition rate between states, I multiplied it by the amount of the corresponding charge transferred, (ΔQ_D), to measure the rate of CT (k^C) for a transition:

$$k^C = \Delta Q_D k^M. \quad (4.1)$$

Both k^C and k^M are obtained in the context of a single transition for one structure. For aid in comparison between structures, these CT rates are summed over all the identified transitions, t , for a given representative structure i , to give a structure-level CT rate constant (K_i^C or K_i^M):

$$K_i^C = \sum_t k_t^C. \quad (4.2)$$

A system-level CT density (ω^C) was then established with a weighted average of K_i^C over the area of the D/A interface in the simulation:

$$\omega^C = \sum_i (K_i^C n_i) \times \frac{1}{A}, \quad (4.3)$$

where n_i was the number of pairs per timestep represented by the structure i from Equation 4.2 and A was the approximate area of the interface (41 nm²).

C. Results

i. Impact of molecular symmetry on DBP/C₇₀ energy landscape

The D/A interface of the DBP/C₇₀ system was represented using 6 alternating layers of 25 DBP or C₇₀ molecules each (shown in Figure 4.1). A large ensemble of interfacial D/A pairs was then obtained. Analysis of the different interfacial pairs was aided by using cylindrical coordinates (shown in Figure 4.2(c)) to represent the location of the center of mass of the C₇₀ molecule relative to the center of mass of the DBP molecule. I focused on two order parameters: first, the distance (Z) from the center of mass of the C₇₀ molecule to the center of mass of the DBP molecule projected on the Z axis, and second, the angle of rotation (Φ) for C₇₀ around the main axis of DBP.

Assessment of the potential of mean force (PMF) using a (Z, Φ) coordinate system [shown in Figure 4.3] reveals a relatively flat energy landscape, with fluctuations of less than $2 kT$. The region of highest probability, located at ($0\text{\AA}, 0^\circ$), had previously been identified as energetically favorable,³¹ but comprised only a small fraction of the overall interface. Other low-energy regions were centered at ($0\text{\AA}, 70^\circ$) and a long vertical region with basins centered at ($9\text{\AA}, 0^\circ$) and ($12\text{\AA}, 60^\circ$). The ridgelines shown in Figure 4.3 divide each of these basins at the crests of highest energy between them using a density-based clustering algorithm.

These four basins reflect the symmetry of the DBP molecule: one long major axis and a shorter minor axis. I utilized a *major-minor* naming scheme that references the position of the C₇₀ molecule **on** a given axis as $[1]$ and **off** it as $[0]$. The representative structures for these basins were therefore referred to as $[1,1]$, $[0,1]$, $[1,0]$, and $[0,0]$. Figure 4.2(b) shows that most interfacial D/A pairs (61%) are in the $[0,0]$ geometry.

Among each these regions, the most probable structure was selected (shown in Figure 4.2(a)) as the representative D/A pair geometry for CT rate analysis.

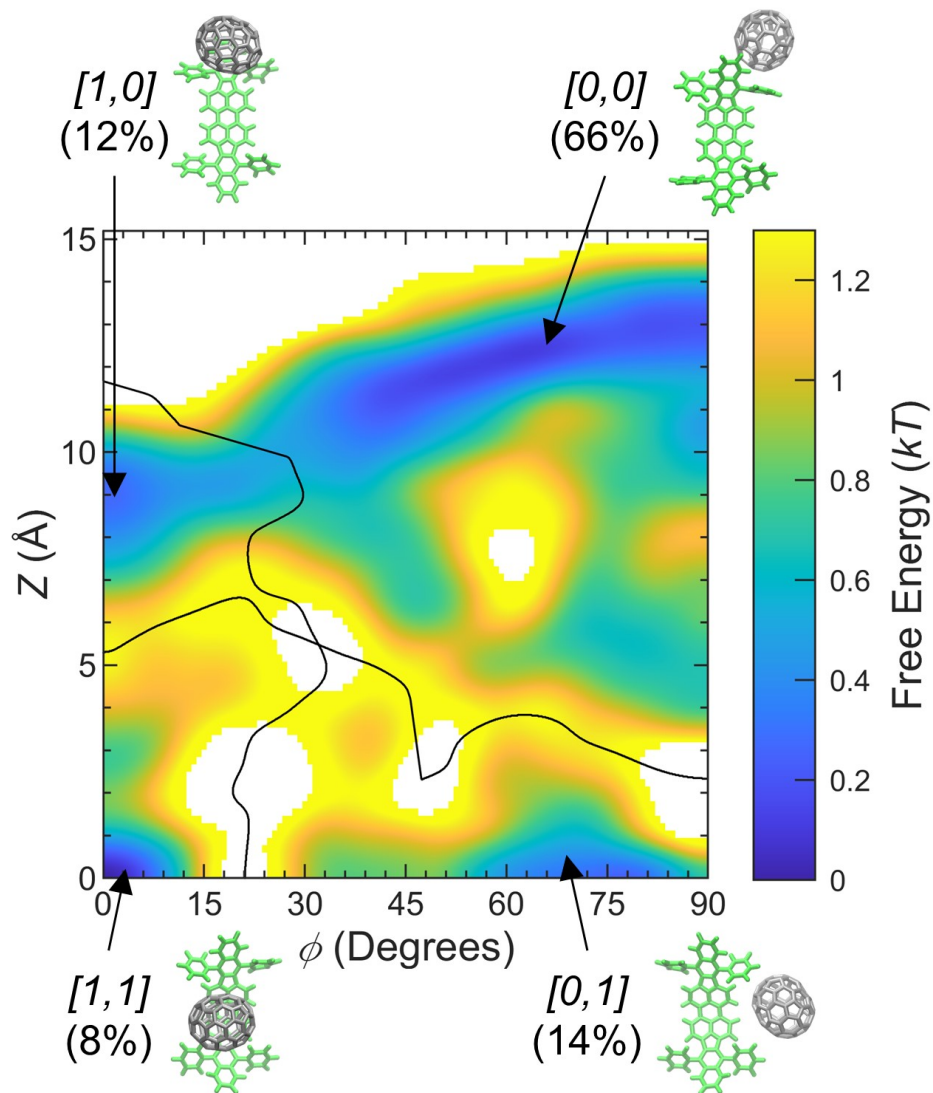


Figure 4.3. The potential of mean force for the DBP/C₇₀ pair on a Z - Φ cylindrical coordinate system. The color is scaled by $k_B T$. Also shown are representative structures ($[1,1]$, $[0,1]$, $[1,0]$, and $[0,0]$) of DBP/C₇₀ pair at each of the four major geometries. Z is the distance of the C₇₀ along the main axis of the DBP molecule from its center and Φ is the angle of rotation around the main axis (see Figure 4.2(c)). The percentage of sampled pairs corresponding to each representative structure is listed next to their label. Solid black lines show the border of each region.

ii. Complex electronic structure of DBP/C₇₀

Electronic structure calculations were then performed on the chosen representative D/A geometries. The important parameters were: (1) the charge of the D/A pair's donor molecule (Q_D), (2) the excitation energy for the D/A pair while isolated in a PCM (E), and (3) the pair's oscillator strength (OS).⁷⁹ These three parameters are shown by the x axis, y axis, and color bar, respectively, in Figure 4.4.

All four geometries contained one excitonic state with an OS significantly higher than all other states from that geometry. This state was denoted as EX1. Transitions studied here were from the EX1 state to each of the dark CT (dCT) states. Each geometry contained a similar number of dCT states (18, 16, 20, and 16 dCT states for $[1,1]$, $[0,1]$, $[1,0]$, and $[0,0]$, respectively) and a single bright state: EX1. The OS of the EX1 state for the $[1,1]$ geometry (0.94) was lower than the OS of the EX1 states for the $[0,1]$, $[1,0]$, and $[0,0]$ geometries (1.24, 1.17, and 1.46) as shown in Figure 4.4.

E for all four EX1 states were similar in magnitude. Moreover, the dCT states for all four geometries had a similar distribution of E . Whereas dCT states for $[0,1]$ and $[0,0]$ predominantly corresponded to the charge transfer of roughly a full electron, many dCT states for $[1,1]$ and $[1,0]$ had much smaller values of Q_D .

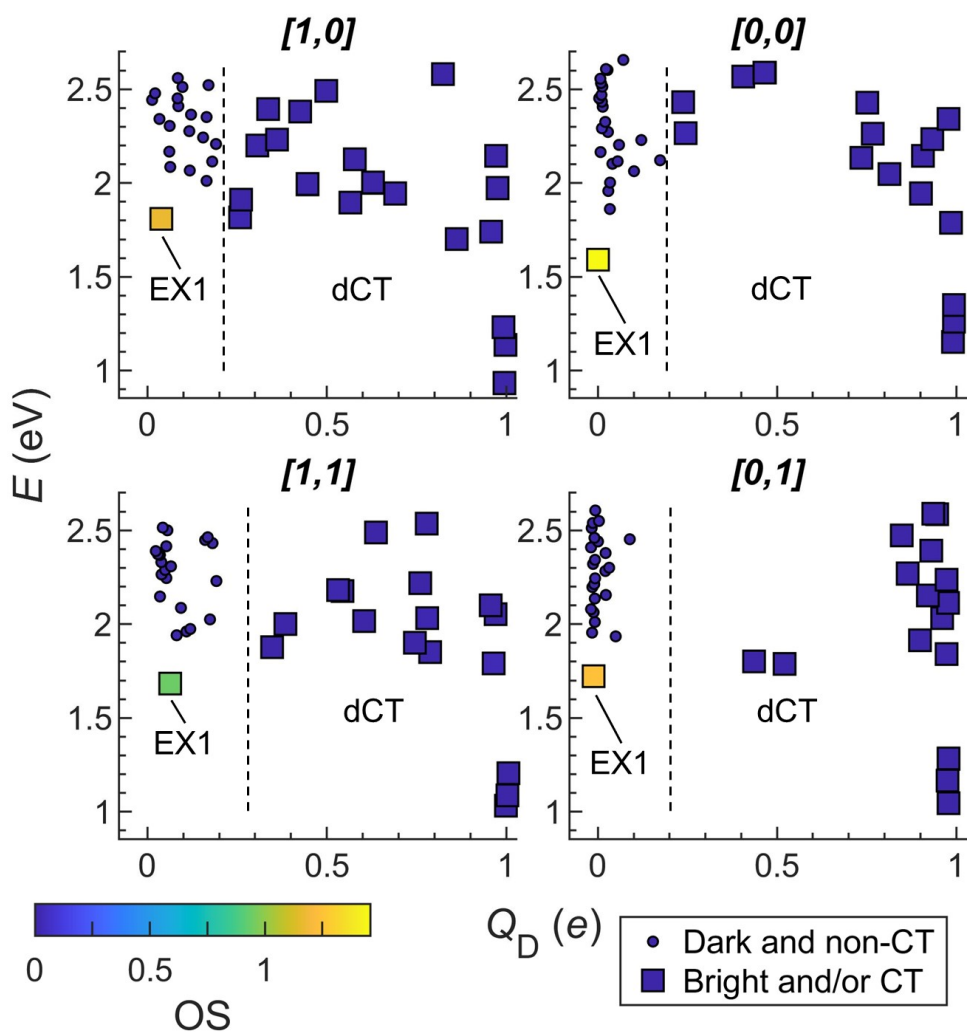


Figure 4.4. Excited state properties of DBP/ C_{70} representative pair geometries. A separate scatter plot with the excitation energy (E) versus the charge of the donor molecule (Q_D) is shown and labelled for each representative geometry. Dots are colored according to their oscillator strength (OS). States used for calculations are shown by large squares while other states are denoted by smaller circles. The dotted line is used to divide the CT states from the non-CT states. The 40 lowest excited states for each geometry are shown.

iii. The $[1,1]$ geometry possesses the fastest rate but lowest population

Next, I calculated the electronic-population-transfer rate constant, k^M , for transitions from a donor state (EX1) to an acceptor state (dCT n). The required inputs to calculate k^M , as shown in Equation 1.1, are the D/A energy-gap first and second moments, the coupling coefficient, Γ_{DA} , and the excitation-energy correction, W_a . k^M increases proportionally to Γ_{DA}^2 but decreases exponentially with increasing $\frac{|<U>|}{\sigma_U}$ (Equation 1.1). The relative energies between states were changed in MD simulations due to the molecular environment. Clearly, the CT states were expected to be stabilized by the condensed-phase polarizable environment more than the localized excitations.⁹⁶

As shown in Figure 4.5, all four geometries contained many transitions with a fast k^M , with $[1,1]$ having six of the seven transitions over 10^{12} Hz. The EX1→dCT10 transition from the $[1,1]$ geometry had the fastest k^M by a factor of five, due to having both a very small $\frac{|<U>|}{\sigma_U}$ and the largest Γ_{DA} . This resulted in the $[1,1]$ geometry having the largest total rate (shown in Figure 4.5 and Table 4.1), represented by K^C which is defined in Equation 4.2. However, K^C for each of the other geometries was only an order of magnitude lower, which allowed each geometry to have an impact on the overall efficiency of the system, dependent on their population as shown in Table 4.1.

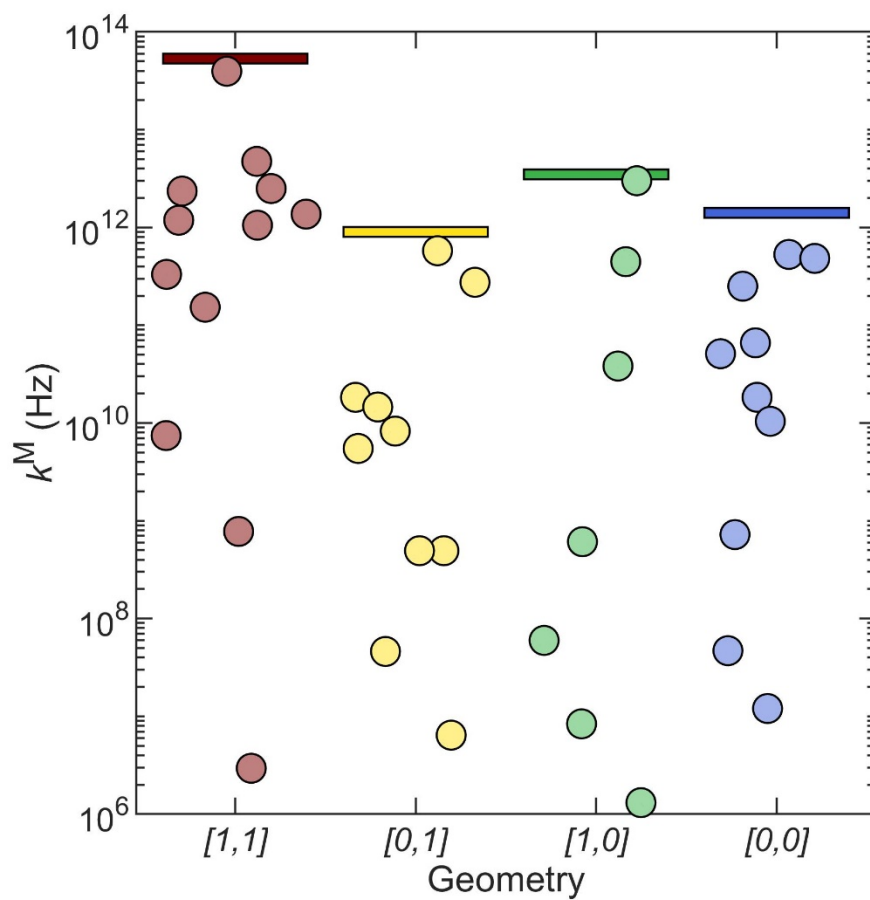


Figure 4.5. Charge transfer rate constants (k^M) for the donor-to-acceptor transitions in each representative DBP/ C_{70} geometry. Each dot represents the CT rate constant of a single transition (e.g., EX1→dCT10). The thin rectangles correspond to the total CT rate constant (K^M) of a geometry. The spacing on the x axis is jittered to allow for easier resolution of each point.

Table 4.1. Charge-transfer rate densities for the four DBP/C₇₀ representative pair geometries

Geometry	Percent of Interface	K^C (nA)	ω^C (nA/nm²)
<i>[1,1]</i>	8.2±0.1%	5520±382	931±65
<i>[0,1]</i>	13.9±0.1%	140± 6	40± 2
<i>[1,0]</i>	12.2±0.1%	503± 52	126±13
<i>[0,0]</i>	65.7±0.1%	206± 3	279± 4
Total			1377±67

D. Discussion

Hundreds of thousands of D/A pairs were sampled from MD simulations of the DBP/C₇₀ interface. Each pair had many intermolecular and intramolecular degrees of freedom. A density-based clustering algorithm utilizing cylindrical symmetry (shown in Figure 4.2(c)) was used to reduce the high dimensionality of the system and classify each pair into one of four regions. Each region corresponded to the placement of the C₇₀ molecule “on” ($[1,1]$) or “off” ($[0,0]$) the major and minor axis (shown in Figure 4.2 (a)) of the DBP molecule. While the $[1,1]$ geometry was the most energetically favorable at a pair-level, Figure 4.3 shows that its region contained the fewest pairs. The $[0,0]$ region contained over half the D/A pairs but also had the most variance in Z and Φ .

A representative pair was chosen for each geometry and the electronic structure was calculated using TD-DFT. CT rate constants, k^M , were calculated between excited states for each molecular pair. By summing k^M for each transition of a geometry and accounting for the quantity of charge transferred, I obtained a structure-level CT rate constant, K^C . Table 4.1 shows that the $[1,1]$ geometry had the highest K^C by an order of magnitude. This higher K^C may have been due to the higher surface area contact between DBP and C₇₀ that comes from being “on” both axes. Each of the other three geometries had a similar K^C . Future studies can use CTRAMER to study the variance of K^C within each region.

However, at a system level, the low population of the $[1,1]$ geometry limited its impact on the overall CT efficiency. To measure this, I used CT rate density, ω^C , which accounted for both the CT rate and the prevalence of a geometry. Table 4.1 showed that $[1,1]$ still had the largest impact on system-level CT, despite its relatively low population. This result suggests that changes in device fabrication that affect the relative population of these geometries has the potential to have a large impact on device performance. $[1,1]$ was the most favorable geometry for CT, however its

low population left room to optimize the fabrication procedure. The greater population of the other geometries allowed them to also have a significant impact on overall CT efficiency.

E. Conclusions

I studied interfacial D/A pairs in a condensed-phase DBP/C₇₀ system and the associated CT across these pairs. I employed the recently introduced¹⁶ CTRAMER software that combines MD simulations and novel TD-DFT methods to aid rate theory in explaining photoinduced CT.

I choose four representative pair geometries using physics-guided machine learning to represent the D/A interface. MD simulations show that the interface was comprised mostly of the *off-off* geometry. The *on-on* geometry, which comprised the smallest portion of the interface, had the fastest CT rate by an order of magnitude. However, the other geometries had transitions with fast enough rates to affect overall CT efficiency due to larger populations.

These results show that a condensed-phase interface can stabilize multiple geometries that have both significant population and CT rate. This illustrated the need for a multi-scale software like CTRAMER that handles both complex many-body effects with MD as well as sophisticated electronic structure methods to accurately calculate long-range CT. I predict that small changes in the molecular morphology of DBP/C₇₀ could have large effects on device performance.

CHAPTER 5. CONCLUSIONS AND FUTURE WORK

In this dissertation I have outlined the main findings of my graduate research about how molecular morphology affects charge-transfer performance in OPV systems. Chapter 1 detailed background information on why research on OPVs is vital as well as the challenges in modelling them using current computational methods. I described the advances in each field that I used for my research as well as my specific research question.

In Chapter 2, I studied the interfacial D-A pairs in a SubPC/C₆₀ OPV system, and the associated CT across these pairs. I employed a comprehensive computational framework combining large-scale MD simulations, state-of-the-art quantum chemistry calculations, and the advanced rate theory of photoinduced CT. Large-scale MD simulations were employed to characterize the interfacial D-A pairs.

I found three categories of pairs, including *on-top*, *hollow*, and *edge*. The *edge* conformation, which had not been addressed in previous studies, was found to dominate the interface. However, the *on top* geometry, which comprised a significantly smaller portion of the interface, was found to have comparable CT rates to the hollow geometry in studies utilizing a polarizable continuum. The molecular resolution invoked here to study the kinetics identified it as promoting the CT process most effectively. This interplay of rate constants and conformational density highlights the scope for improving the ability of controlling the fabrication at the molecular level. I predict that increasing the relative weight of *on-top* conformational pairs achieves enhanced CT kinetics across the interface.

In Chapter 3, I described the software package CTRAMER for the analysis of CT rates based on electronic structure calculations, MD simulations, and rate theory. CTRAMER is a unique combination of well-established methods from different disciplines that allows for a more precise

study of photoinduced CT between excited states and explicit environment. The customizable features, software architecture, and guidelines for usage were discussed. Additionally, the scientific justification behind the different approaches as well as example results were described.

CTRAMER will continue to be actively developed and supported, as it will remain a long-term focus of my collaborators. Additions planned for the immediate future are automated tuning of the parameters for electronic structure calculations, enabling different level of theory, and machine-learning clustering methods for selecting representative structures. Other future goals include various extensions to improve the accessibility and computational efficiency of the software.

In Chapter 4 I described how hundreds of thousands of D/A pairs were sampled from MD simulations of the DBP/C₇₀ interface. Each pair had many intermolecular and intramolecular degrees of freedom. A density-based clustering algorithm utilizing cylindrical symmetry was used to reduce the high dimensionality of the system and classify each pair into one of four regions. While the $[1,1]$ geometry was the most energetically favorable at a pair-level, it contained the fewest pairs. The $[1,1]$ geometry also had the highest K^C by an order of magnitude. This higher K^C may have been due to the higher surface area contact between DBP and C₇₀ that comes from being “on” both axes. Each of the other three geometries had a similar K^C . However, at a system level, the low population of the $[1,1]$ geometry limited its impact on the overall CT efficiency. The greater population of the other geometries allowed them to also have a significant impact on overall CT efficiency.

These results show that a condensed-phase interface can stabilize multiple geometries that have both a significant population and a fast CT rate. Future studies can use CTRAMER to study the variance of K^C within each region. This finding illustrates the need for a multi-scale software like

CTRAMER, which handles complex many-body effects with MD and the sophisticated electronic structure methods needed to accurately calculate long-range CT. I predict that small changes in the molecular morphology of DBP/C₇₀ will have large effects on device performance.

There are many avenues to expand on these results using CTRAMER, but three are of particular interest. First, applying the CTRAMER process and software to systems other than SubPC/C₆₀ and DBP/C₇₀. There are many other types of OPV systems to explore such as non-fullerene acceptors,^{10,109} polymer systems^{19,34,93} and hybrid cells.² Additionally CTRAMER can be used to study CT in biological systems.⁷⁵

A second area of interest is using CTRAMER to study the systems in this dissertation in greater depth. While the use of representative geometries is a step forward from optimized geometries, there is still a large amount of variance within the regions they represent (particularly in the SubPC/C₆₀ *edge* geometry and the DBP/C₇₀ *[0,0]* geometry). It remains to be shown how this translates to variance in CT rate within these regions. A substantially larger number of representative geometries would allow for the use of machine learning algorithms to predict the CT rate of geometries. To aid this, a more computationally efficient alternative to TD-DFT would also need to be developed.

A last area of interest would be to anchor these CT results into the other primary processes. These processes include charge diffusion,^{4,5,11,96,107} dissociation,^{29,108,109} and recombination,^{5,11,109-111} which are associated with a wide range of length and time scales.^{9,11,105-108,110,112-114} While there appears to be evidence that interfacial CT plays a central role in determining the overall device performance, particularly in the tested systems,^{8,23,97} all of the rates of each step should be determined without imposing any assumptions.^{14,15} A possible method of accounting for these differing scales would be the developed of a kinetic Monte Carlo method integrated into CTRAMER.

BIBLIOGRAPHY

1. Fraunhofer ISE. Photovoltaics Report, updated: 27 July 2021.
2. Green MA, *et al.* Solar cell efficiency tables (Version 58). *Prog Photovoltaics* **29**, 657-667 (2021).
3. Tinnin J, *et al.* Molecular-Level Exploration of the Structure-Function Relations Underlying Interfacial Charge Transfer in the Subphthalocyanine/C60 Organic Photovoltaic System. *Phys Rev Appl* **13**, 11 (2020).
4. Lee MH, Geva E, Dunietz BD. Calculation from First-Principles of Golden Rule Rate Constants for Photoinduced Subphthalocyanine/Fullerene Interfacial Charge Transfer and Recombination in Organic Photovoltaic Cells. *J Phys Chem C* **118**, 9780-9789 (2014).
5. Zhao Y, Liang W. Charge transfer in organic molecules for solar cells: theoretical perspective. *Chem Soc Rev* **41**, 1075-1087 (2012).
6. Kim J, Yim S. Influence of surface morphology evolution of SubPc layers on the performance of SubPc/C-60 organic photovoltaic cells. *Appl Phys Lett* **99**, 193303 (2011).
7. Tian H, Yu Z, Hagfeldt A, Kloo L, Sun L. Organic Redox Couples and Organic Counter Electrode for Efficient Organic Dye-Sensitized Solar Cells. *J Am Chem Soc* **133**, 9413-9422 (2011).
8. Tong X, Lassiter BE, Forrest SR. Inverted organic photovoltaic cells with high open-circuit voltage. *Org Electron* **11**, 705-709 (2010).
9. Hagfeldt A, Boschloo G, Sun L, Kloo L, Pettersson H. Dye-Sensitized Solar Cells. *Chemical Reviews* **110**, 6595-6663 (2010).
10. Wang T, Bredas J-L. Organic Solar Cells Based on Non-fullerene Small-Molecule Acceptors: Impact of Substituent Position. *Matter* **2**, 119-135 (2020).
11. Kurpiers J, *et al.* Probing the pathways of free charge generation in organic bulk heterojunction solar cells. *Nature Communications* **9**, 2038 (2018).
12. Falke SM, *et al.* Coherent ultrafast charge transfer in an organic photovoltaic blend. *Science* **344**, 1001-1005 (2014).
13. Benatto L, *et al.* Comparing C-60 and C-70 as acceptor in organic solar cells: Influence of the electronic structure and aggregation size on the photovoltaic characteristics. *Thin Solid Films* **697**, 137827 (2020).
14. Giebink NC, Wiederrecht GP, Wasielewski MR, Forrest SR. Ideal diode equation for organic heterojunctions. I. Derivation and application. *Physical Review B* **82**, 155305 (2010).

15. Giebink NC, Wiederrecht GP, Wasielewski MR, Forrest SR. Thermodynamic efficiency limit of excitonic solar cells. *Physical Review B* **83**, 195326 (2011).
16. Tinnin J, *et al.* CTRAMER: An open-source software package for correlating interfacial charge transfer rate constants with donor/acceptor geometries in organic photovoltaic materials. *The Journal of Chemical Physics* **154**, 214108 (2021).
17. Yoshikawa K, *et al.* Silicon heterojunction solar cell with interdigitated back contacts for a photoconversion efficiency over 26%. *Nature Energy* **2**, 17032 (2017).
18. Lee MH, Dunietz BD, Geva E. Donor-to-Donor vs Donor-to-Acceptor Interfacial Charge Transfer States in the Phthalocyanine-Fullerene Organic Photovoltaic System. *J Phys Chem Lett* **5**, 3810-3816 (2014).
19. Balamurugan D, *et al.* Multiscale Simulation of the Ground and Photo-Induced Charge-Separated States of a Molecular Triad in Polar Organic Solvent: Exploring the Conformations, Fluctuations, and Free Energy Landscapes. *J Phys Chem B* **117**, 12065-12075 (2013).
20. Brédas J-L, Beljonne D, Coropceanu V, Cornil J. Charge-Transfer and Energy-Transfer Processes in π -Conjugated Oligomers and Polymers: A Molecular Picture. *Chemical Reviews* **104**, 4971-5004 (2004).
21. D’Innocenzo V, *et al.* Excitons versus free charges in organo-lead tri-halide perovskites. *Nature Communications* **5**, 3586 (2014).
22. Tang CW, VanSlyke SA. Organic Electroluminescent Diodes. *Appl Phys Lett*, 913 (1987).
23. Ilyas N, *et al.* Sticking with the Pointy End? Molecular Configuration of Chloro Boron-Subphthalocyanine on Cu(111). *J Phys Chem C* **120**, 7113-7121 (2016).
24. Mutolo KL, Mayo EI, Rand BP, Forrest SR, Thompson ME. Enhanced Open-Circuit Voltage in Subphthalocyanine/C60 Organic Photovoltaic Cells. *J Am Chem Soc* **128**, 8108-8109 (2006).
25. D’Avino G, *et al.* Electrostatic phenomena in organic semiconductors: fundamentals and implications for photovoltaics. *Journal of Physics: Condensed Matter* **28**, 433002 (2016).
26. Josey DS, *et al.* Outdoor Performance and Stability of Boron Subphthalocyanines Applied as Electron Acceptors in Fullerene-Free Organic Photovoltaics. *ACS Energy Letters* **2**, 726-732 (2017).
27. Pandey R, Gunawan AA, Mkhoyan KA, Holmes RJ. Efficient Organic Photovoltaic Cells Based on Nanocrystalline Mixtures of Boron Subphthalocyanine Chloride and C60. *Advanced Functional Materials* **22**, 617-624 (2012).

28. Wilcox DE, *et al.* Ultrafast Charge-Transfer Dynamics at the Boron Subphthalocyanine Chloride/C60 Heterojunction: Comparison between Experiment and Theory. *The journal of physical chemistry letters* **6** 3, 569-575 (2015).
29. Yi YP, Coropceanu V, Bredas JL. Exciton-Dissociation and Charge-Recombination Processes in Pentacene/C-60 Solar Cells: Theoretical Insight into the Impact of Interface Geometry. *J Am Chem Soc* **131**, 15777-15783 (2009).
30. Morris SE, University of Michigan, 2014.
31. Song Y, *et al.* Efficient Charge Generation via Hole Transfer in Dilute Organic Donor–Fullerene Blends. *The Journal of Physical Chemistry Letters* **11**, 2203-2210 (2020).
32. Xiao X, Zimmerman JD, Lassiter BE, Bergemann KJ, Forrest SR. A hybrid planar-mixed tetraphenyldibenzoperiflanthene/C-70 photovoltaic cell. *Appl Phys Lett* **102**, (2013).
33. Lee MH, Geva E, Dunitz BD. The Effect of Interfacial Geometry on Charge-Transfer States in the Phthalocyanine/Fullerene Organic Photovoltaic System. *J Phys Chem A* **120**, 2970-2975 (2016).
34. Han J, *et al.* On the Interplay between Electronic Structure and Polarizable Force Fields When Calculating Solution-Phase Charge-Transfer Rates. *J Chem Theory Comput* **16**, 6481-6490 (2020).
35. Wang J, Wang W, Kollman PA, Case DA. Automatic atom type and bond type perception in molecular mechanical calculations. *J Mol Graph* **25**, 247-260 (2006).
36. Wang J, Wolf RM, Caldwell JW, Kollman PA, Case DA. Development and testing of a general amber force field. *J Comput Chem* **25**, 1157-1174 (2004).
37. Case DA, *et al.* (2012), *AMBER 12*. University of California, San Francisco
38. Case DA, *et al.* (2014), *AMBER 14*. University of California, San Francisco
39. Ciccotti G, Ryckaert JP. Molecular-Dynamics Simulation of Rigid Molecules. *Computer Physics Reports* **4**, 346-392 (1986).
40. Darden T, York D, Pedersen L. Particle Mesh Ewald - An N.Log(N) Method for Ewald Sums in Large Systems. *J Chem Phys* **98**, 10089-10092 (1993).
41. York DM, Darden TA, Pedersen LG. The effect of long-range electrostatic interactions in simulations of macromolecular crystals: A comparison of the Ewald and truncated list methods. *The Journal of Chemical Physics* **99**, 8345-8348 (1993).
42. Peter D H. Kernel estimation of a distribution function. *Communications in Statistics - Theory and Methods* **14**, 605-620 (1985).

43. Bowman A, Azzalini A. Applied smoothing techniques for data analysis : the kernel approach with S-plus illustrations. *Journal of the American Statistical Association* **94**, 982 (1999).
44. Shimazaki H, Shinomoto S. Kernel bandwidth optimization in spike rate estimation. *Journal of Computational Neuroscience* **29**, 171-182 (2010).
45. Silverman BW. *Density estimation for statistics and data analysis / B.W. Silverman.* Chapman and Hall (1986).
46. Dirac PAM. Note on Exchange Phenomena in the Thomas Atom. *Mathematical Proceedings of the Cambridge Philosophical Society* **26**, 376-385 (2008).
47. Hohenberg P, Kohn W. Inhomogeneous Electron Gas. *Physical Review* **136**, B864-B871 (1964).
48. Kohn W, Becke AD, Parr RG. Density Functional Theory of Electronic Structure. *The Journal of Physical Chemistry* **100**, 12974-12980 (1996).
49. Kohn W, Sham LJ. Self-Consistent Equations Including Exchange and Correlation Effects. *Physical Review* **140**, A1133-A1138 (1965).
50. Pople JA, Gill PMW, Johnson BG. Kohn—Sham density-functional theory within a finite basis set. *Chem Phys Lett* **199**, 557-560 (1992).
51. Ziegler T. Approximate density functional theory as a practical tool in molecular energetics and dynamics. *Chemical Reviews* **91**, 651-667 (1991).
52. Shao Y, *et al.* Advances in methods and algorithms in a modern quantum chemistry program package. *Physical Chemistry Chemical Physics* **8**, 3172-3191 (2006).
53. Runge E, Gross EKV. Density-Functional Theory for Time-Dependent Systems. *Phys Rev Lett* **52**, 997-1000 (1984).
54. Dreuw A, Head-Gordon M. Single-Reference ab Initio Methods for the Calculation of Excited States of Large Molecules. *Chemical Reviews* **105**, 4009-4037 (2005).
55. Perdew JP, *et al.* Prescription for the design and selection of density functional approximations: More constraint satisfaction with fewer fits. *The Journal of Chemical Physics* **123**, 062201 (2005).
56. Perdew JP, Schmidt K. Jacob's ladder of density functional approximations for the exchange-correlation energy. In: *International Conference on Density Functional Theory and its Applications to Materials* (2000).
57. Becke AD. Density-functional thermochemistry. III. The role of exact exchange. *The Journal of Chemical Physics* **98**, 5648-5652 (1993).

58. Stephens PJ, Devlin FJ, Chabalowski CF, Frisch MJ. Ab Initio Calculation of Vibrational Absorption and Circular Dichroism Spectra Using Density Functional Force Fields. *The Journal of Physical Chemistry* **98**, 11623-11627 (1994).
59. Marshburn RD, *et al.* Are all charge-transfer parameters created equally? A study of functional dependence and excited-state charge-transfer quantification across two dye families. *Physical Chemistry Chemical Physics* **23**, 20583-20597 (2021).
60. Lange AW, Herbert JM. Both Intra- and Interstrand Charge-Transfer Excited States in Aqueous B-DNA Are Present at Energies Comparable To, or Just Above, the $1\pi\pi^*$ Excitonic Bright States. *J Am Chem Soc* **131**, 3913-3922 (2009).
61. Lange A, Herbert JM. Simple Methods To Reduce Charge-Transfer Contamination in Time-Dependent Density-Functional Calculations of Clusters and Liquids. *J Chem Theory Comput* **3**, 1680-1690 (2007).
62. Lange AW, Rohrdanz MA, Herbert JM. Charge-transfer excited states in a pi-stacked adenine dimer, as predicted using long-range-corrected time-dependent density functional theory. *The journal of physical chemistry B* **112**, 6304-6308 (2008).
63. Chai JD, Head-Gordon M. Systematic optimization of long-range corrected hybrid density functionals. *J Chem Phys* **128**, 084106 (2008).
64. Chai J-D, Head-Gordon M. Long-range corrected hybrid density functionals with damped atom–atom dispersion corrections. *Physical Chemistry Chemical Physics* **10**, 6615-6620 (2008).
65. Rohrdanz MA, Herbert JM. Simultaneous benchmarking of ground- and excited-state properties with long-range-corrected density functional theory. *The Journal of Chemical Physics* **129**, 034107 (2008).
66. Rohrdanz MA, Martins KM, Herbert JM. A long-range-corrected density functional that performs well for both ground-state properties and time-dependent density functional theory excitation energies, including charge-transfer excited states. *The Journal of Chemical Physics* **130**, 054112 (2009).
67. Baer R, Neuhauser D. Density functional theory with correct long-range asymptotic behavior. *Phys Rev Lett* **94**, 043002 (2005).
68. Livshits E, Baer R. A well-tempered density functional theory of electrons in molecules. *Physical Chemistry Chemical Physics* **9**, 2932-2941 (2007).
69. Stein T, Kronik L, Baer R. Prediction of charge-transfer excitations in coumarin-based dyes using a range-separated functional tuned from first principles. *J Am Chem Soc* **131**, 002818-002820 (2009).
70. Baer R, Livshits E, Salzner U. Tuned Range-Separated Hybrids in Density Functional Theory. *Annual Review of Physical Chemistry* **61**, 85-109 (2010).

71. Salzner U, Baer R. Koopmans' springs to life. *The Journal of Chemical Physics* **131**, 231101 (2009).
72. Bhandari S, Cheung MS, Geva E, Kronik L, Dunietz BD. Fundamental Gaps of Condensed-Phase Organic Semiconductors from Single-Molecule Calculations using Polarization-Consistent Optimally Tuned Screened Range-Separated Hybrid Functionals. *J Chem Theory Comput* **14**, 6287-6294 (2018).
73. Refaely-Abramson S, *et al.* Gap renormalization of molecular crystals from density-functional theory. *Physical Review B* **88**, 081204 (2013).
74. Zheng Z, Egger DA, Brédas J-L, Kronik L, Coropceanu V. Effect of Solid-State Polarization on Charge-Transfer Excitations and Transport Levels at Organic Interfaces from a Screened Range-Separated Hybrid Functional. *The Journal of Physical Chemistry Letters* **8**, 3277-3283 (2017).
75. Aksu H, Schubert A, Geva E, Dunietz BD. Explaining Spectral Asymmetries and Excitonic Characters of the Core Pigment Pairs in the Bacterial Reaction Center Using a Screened Range-Separated Hybrid Functional. *J Phys Chem B* **123**, 8970-8975 (2019).
76. Begam K, Bhandari S, Maiti B, Dunietz BD. Screened Range-Separated Hybrid Functional with Polarizable Continuum Model Overcomes Challenges in Describing Triplet Excitations in the Condensed Phase Using TDDFT. *J Chem Theory Comput* **16**, 3287-3293 (2020).
77. Bhandari S, Dunietz BD. Quantitative Accuracy in Calculating Charge Transfer State Energies in Solvated Molecular Complexes Using a Screened Range Separated Hybrid Functional within a Polarized Continuum Model. *J Chem Theory Comput* **15**, 4305-4311 (2019).
78. Lee MH, Dunietz BD, Geva E. Calculation from First Principles of Intramolecular Golden-Rule Rate Constants for Photo-Induced Electron Transfer in Molecular Donor- Acceptor Systems. *J Phys Chem C* **117**, 23391-23401 (2013).
79. Robinson JW. *Atomic Spectroscopy*, 2nd edn. Marcel Dekker, Inc. (1996).
80. Voityuk AA, Rosch N. Fragment charge difference method for estimating donor-acceptor electronic coupling: Application to DNA pi-stacks. *J Chem Phys* **117**, 5607-5616 (2002).
81. Barbara PF, Meyer TJ, Ratner MA. Contemporary issues in electron transfer research. *J Phys Chem* **100**, 13148-13168 (1996).
82. Marcus RA. On the Theory of Oxidation-Reduction Reactions Involving Electron Transfer. *J Chem Phys* **24**, 966-978 (1956).
83. Marcus RA. Electrostatic Free Energy and Other Properties of States Having Nonequilibrium Polarization. *J Chem Phys* **24**, 979-989 (1956).

84. Marcus RA. Electron-Transfer Reactions in Chemistry - Theory and Experiment. *Rev Mod Phys* **65**, 599-610 (1993).
85. Sun X, *et al.* Computational Study of Charge-Transfer Dynamics in the Carotenoid-Porphyrin-C-60 Molecular Triad Solvated in Explicit Tetrahydrofuran and Its Spectroscopic Signature. *J Phys Chem C* **122**, 11288-11299 (2018).
86. Sun X, Geva E. Equilibrium Fermi's Golden Rule Charge Transfer Rate Constants in the Condensed Phase: The Linearized Semiclassical Method vs Classical Marcus Theory. *J Phys Chem A* **120**, 2976-2990 (2016).
87. Leggett AJ, *et al.* Dynamics of the dissipative two-state system. *Rev Mod Phys* **59**, 1-85 (1987).
88. Makri N. The Linear Response Approximation and Its Lowest Order Corrections: An Influence Functional Approach. *The Journal of Physical Chemistry B* **103**, 2823-2829 (1999).
89. Cao J, Voth GA. Modeling physical systems by effective harmonic oscillators: The optimized quadratic approximation. *The Journal of Chemical Physics* **102**, 3337-3348 (1995).
90. Tong Z, *et al.* Charge transfer rate constants for the carotenoid-porphyrin-C-60 molecular triad dissolved in tetrahydrofuran: The spin-boson model vs the linearized semiclassical approximation. *J Chem Phys* **153**, 044105 (2020).
91. Shi Q, Geva E. Nonradiative Electronic Relaxation Rate Constants from Approximations Based on Linearizing the Path-Integral Forward-Backward Action. *The Journal of Physical Chemistry A* **108**, 6109-6116 (2004).
92. Sun X, Geva E. Nonequilibrium Fermi's Golden Rule Charge Transfer Rates via the Linearized Semiclassical Method. *J Chem Theory Comput* **12**, 2926-2941 (2016).
93. Hu Z, *et al.* Photoinduced Charge Transfer Dynamics in the Carotenoid-Porphyrin-C-60 Triad via the Linearized Semiclassical Nonequilibrium Fermi's Golden Rule. *J Phys Chem B* **124**, 9579-9591 (2020).
94. Sun X, Geva E. Non-Condon equilibrium Fermi's golden rule electronic transition rate constants via the linearized semiclassical method. *J Chem Phys* **144**, 244105 (2016).
95. Sun X, Geva E. Non-Condon nonequilibrium Fermi's golden rule rates from the linearized semiclassical method. *J Chem Phys* **145**, 064109 (2016).
96. Manna AK, Balamurugan D, Cheung MS, Dunitz BD. Unraveling the Mechanism of Photoinduced Charge Transfer in Carotenoid-Porphyrin-C-60 Molecular Triad. *J Phys Chem Lett* **6**, 1231-1237 (2015).

97. Stadler C, Hansen S, Kroger I, Kumpf C, Umbach E. Tuning intermolecular interaction in long-range-ordered submonolayer organic films. *Nat Phys* **5**, 153-158 (2009).
98. Martinez L, Andrade R, Birgin EG, Martinez JM. PACKMOL: A Package for Building Initial Configurations for Molecular Dynamics Simulations. *J Comput Chem* **30**, 2157-2164 (2009).
99. Claessens CG, González-Rodríguez D, Torres T. Subphthalocyanines: Singular Nonplanar Aromatic Compounds Synthesis, Reactivity, and Physical Properties. *Chemical Reviews* **102**, 835-854 (2002).
100. Wu X, Liu Z, Huang S, Wang W. Molecular dynamics simulation of room-temperature ionic liquid mixture of [bmim][BF₄] and acetonitrile by a refined force field. *Physical Chemistry Chemical Physics* **7**, 2771-2779 (2005).
101. Kullback S. The Kullback-Leibler Distance. *Am Stat* **41**, 340-340 (1987).
102. Weinkam P, Pletneva EV, Gray HB, Winkler JR, Wolynes PG. Electrostatic effects on funneled landscapes and structural diversity in denatured protein ensembles. *Proceedings of the National Academy of Sciences* **106**, 1796-1801 (2009).
103. Rassolov VA, Pople JA, Ratner MA, Windus TL. 6-31G* basis set for atoms K through Zn. *J Chem Phys* **109**, 1223-1229 (1998).
104. Morris SE, *et al.* Effect of axial halogen substitution on the performance of subphthalocyanine based organic photovoltaic cells. *Org Electron* **15**, 3660-3665 (2014).
105. Xiao MY, Tian YP, Zheng SH. An insight into the relationship between morphology and open circuit voltage/electronic absorption spectrum at donor-acceptor interface in boron subphthalocyanine chloride/C70 solar cell: A DFT/TDDFT exploration. *Org Electron* **59**, 279-287 (2018).
106. Jackson NE, Savoie BM, Marks TJ, Chen LX, Ratner MA. The Next Breakthrough for Organic Photovoltaics? *J Phys Chem Lett* **6**, 77-84 (2015).
107. Jones ML, Jankowski E. Computationally connecting organic photovoltaic performance to atomistic arrangements and bulk morphology. *Mol Simul* **43**, 756-773 (2017).
108. Heitzer HM, Savoie BM, Marks TJ, Ratner MA. Organic Photovoltaics: Elucidating the Ultra-Fast Exciton Dissociation Mechanism in Disordered Materials. *Angew Chem-Int Edit* **53**, 7456-7460 (2014).
109. Causa M, *et al.* The fate of electron-hole pairs in polymer:fullerene blends for organic photovoltaics. *Nature Communications* **7**, 12556 (2016).
110. Teuscher J, *et al.* Charge separation and carrier dynamics in donor-acceptor heterojunction photovoltaic systems. *Struct Dyn* **4**, 061503-061503 (2017).

111. Brédas J-L, Norton JE, Cornil J, Coropceanu V. Molecular Understanding of Organic Solar Cells: The Challenges. *Accounts of Chemical Research* **42**, 1691-1699 (2009).
112. Hedley GJ, *et al.* Determining the optimum morphology in high-performance polymer-fullerene organic photovoltaic cells. *Nature Communications* **4**, (2013).
113. Liu Y, *et al.* Aggregation and morphology control enables multiple cases of high-efficiency polymer solar cells. *Nature Communications* **5**, 5293 (2014).
114. Docampo P, Ball JM, Darwich M, Eperon GE, Snaith HJ. Efficient organometal trihalide perovskite planar-heterojunction solar cells on flexible polymer substrates. *Nature Communications* **4**, 2761 (2013).
115. Phillips H, Geva E, Dunietz BD. Calculating Off-Site Excitations in Symmetric Donor–Acceptor Systems via Time-Dependent Density Functional Theory with Range-Separated Density Functionals. *J Chem Theory Comput* **8**, 2661-2668 (2012).
116. Phillips H, Zheng Z, Geva E, Dunietz BD. Orbital gap predictions for rational design of organic photovoltaic materials. *Org Electron* **15**, 1509-1520 (2014).
117. Zheng S, Phillips H, Geva E, Dunietz BD. Ab Initio Study of the Emissive Charge-Transfer States of Solvated Chromophore-Functionalized Silsesquioxanes. *J Am Chem Soc* **134**, 6944-6947 (2012).
118. Steffen MA, Lao K, Boxer SG. Dielectric Asymmetry in the Photosynthetic Reaction-Center. *Science* **264**, 810-816 (1994).
119. Niedringhaus A, *et al.* Primary processes in the bacterial reaction center probed by two-dimensional electronic spectroscopy. *Proc Natl Acad Sci U S A* **115**, 3563-3568 (2018).
120. Koepke J, *et al.* pH modulates the quinone position in the photosynthetic reaction center from *Rhodobacter sphaeroides* in the neutral and charge separated states. *J Mol Biol* **371**, 396-409 (2007).
121. Tinnin J, *et al.*, 2021, CTRAMER SubPC/C60 Data, Github, <https://github.com/ctramer/ctramer>
122. Xu C, Li G, Zheng S. Exploring the effects of axial halogen substitutions of subphthalocyanine on the charge transfer nature in subPC/C60 solar cells. *Journal of Photochemistry and Photobiology A: Chemistry* **403**, 112852 (2020).
123. Lüftner D, *et al.* Experimental and theoretical electronic structure of quinacridone. *Physical Review B* **90**, 075204 (2014).
124. Truong TN, Stefanovich EV. A new method for incorporating solvent effect into the classical, ab initio molecular orbital and density functional theory frameworks for arbitrary shape cavity. *Chem Phys Lett* **240**, 253-260 (1995).

125. Tomasi J, Mennucci B, Cammi R. Quantum Mechanical Continuum Solvation Models. *Chemical Reviews* **105**, 2999-3094 (2005).